Title
BTG1 mutation yields supercompetitive B cells primed for malignant transformation.

Journal
Science, 379(6629)

Authors
Mlynarczyk, Coraline
Teater, Matt
Pae, Juhee
et al.

Publication Date
2023-01-20

DOI
10.1126/science.abj7412

Peer reviewed

HHS Public Access

Author manuscript

Science. Author manuscript; available in PMC 2023 September 22.

Published in final edited form as:

Science. 2023 January 20; 379(6629): eabj7412. doi:10.1126/science.abj7412.

BTG1 mutation yields supercompetitive B cells primed for malignant transformation

Coraline Mlynarczyk[1,*], **Matt Teater**[1], **Juhee Pae**[2], **Christopher R. Chin**[1,3,4,5], **Ling Wang**[1], **Theinmozhi Arulraj**[6], **Darko Barisic**[1], **Antonin Papin**[7], **Kenneth B. Hoehn**[8], **Ekaterina Kots**[9], **Jonatan Ersching**[2,†], **Arnab Bandyopadhyay**[6], **Ersilia Barin**[10], **Hui Xian Poh**[10], **Chiara M. Evans**[11,12], **Amy Chadburn**[7], **Zhengming Chen**[13], **Hao Shen**[1], **Hannah M. Isles**[1], **Benedikt Pelzer**[1], **Ioanna Tsialta**[1], **Ashley S. Doane**[1,5], **Huimin Geng**[14], **Muhammad Hassan Rehman**[1,15], **Jonah Melnick**[1], **Wyatt Morgan**[1,‡], **Diu T. T. Nguyen**[11,16], **Olivier Elemento**[3,17], **Michael G. Kharas**[11], **Samie R. Jaffrey**[10], **David W. Scott**[18], **George Khelashvili**[5,9], **Michael Meyer-Hermann**[6,19], **Gabriel D. Victora**[2], **Ari Melnick**[1,*]

[1]Division of Hematology and Oncology, Department of Medicine and Meyer Cancer Center, Weill Cornell Medicine, New York, NY, USA.

[2]Laboratory of Lymphocyte Dynamics, The Rockefeller University, New York, NY, USA.

[3]Department of Physiology and Biophysics, Weill Cornell Medicine, New York, NY, USA.

[4]Tri-Institutional PhD Program in Computational Biomedicine, New York, NY, USA.

[5]Institute for Computational Biomedicine, Weill Cornell Medicine, New York, NY, USA.

[6]Department of Systems Immunology and Braunschweig Integrated Centre of Systems Biology (BRICS), Helmholtz Centre for Infection Research, Braunschweig, Germany.

[7]Department of Pathology and Laboratory Medicine, Weill Cornell Medicine, New York, NY, USA.

[8]Department of Pathology, Yale School of Medicine, New Haven, CT, USA.

[*]Corresponding author. chm2065@med.cornell.edu (C.M.); amm2014@med.cornell.edu (A.M.).

[‡]Present address: Gordian Biotechnology, San Francisco, CA, USA.

[†]Deceased.

Author contributions: Conceptualization: C.M. and A.M. Data curation: M.T., C.R.C., Z.C., and A.S.D. Formal analysis: C.M., M.T., J.P., C.R.C,. T.A., D.B., A.P., K.B.H., J.E., E.K., A.B., E.B., H.X.P., A.C., Z.C., H.M.I., B.P., I.T., D.T.T.N., A.S.D., H.G., M.H.R., J.M., W.M., and G.K. Funding acquisition: C.M., A.M., G.D.V., and O.E. Investigation: C.M., J.P., L.W., D.B., A.P., J.E., E.B., H.X.P., C.M.E., H.M.I., B.P., I.T., H.S., D.T.T.N., M.H.R., and W.M. Methodology: C.M., J.P., A.P., J.E., E.B., H.X.P., C.M.E., H.M.I., B.P., D.T.T.N., M.G.K., S.R.J., G.D.V., and A.M. Resources: O.E., M.G.K., D.W.S., S.R.J., M.M.-H., G.K., G.D.V., and A.M. Software: M.T., C.R.C., T.A., K.B.H., E.K., A.B., Z.C., A.S.D., H.G., M.M.-H., and G.K. Supervision: A.M. and G.D.V. Validation: C.M., M.T., J.P., C.R.C., L.W., T.A., J.E., D.B., A.P., K.B.H., E.K., A.B., E.B., H.X.P., C.M.E., A.C., Z.C., H.M.I., B.P., I.T., GC, and A.M. Visualization: C.M., J.P., M.T., C.R.C., T.A., K.B.H., E.K., A.C., Z.C., H.M.I., A.S.D., and A.M. Writing – original draft: C.M. and A.M. Writing – review & editing: C.M., M.T., J.P., C.R.C., L.W., T.A., D.B., A.P., K.B.H., E.K., J.E., A.B., E.B., H.X.P., C.M.E., A.C., Z.C., H.S., H.M.I., B.P., I.T., A.S.D., H.G., M.H.R., J.M., W.M., D.T.T.N., O.E., M.G.K., S.R.J., D.W.S., G.K., M.M.-H., G.D.V., and A.M.

SUPPLEMENTARY MATERIALS

science.org/doi/10.1126/science.abj7412

Figs. S1 to S16

Tables S1 to S8

MDAR Reproducibility Checklist

View/request a protocol for this paper from Bio-protocol.

[9]Department of Physiology and Biophysics, Weill Cornell Medicine, New York, NY, USA.

[10]Department of Pharmacology and Meyer Cancer Center, Weill Cornell Medicine, New York, NY, USA.

[11]Molecular Pharmacology Program and Center for Cell Engineering, Center for Stem Cell Biology, Center for Experimental Therapeutics, and Center for Hematologic Malignancies, Memorial Sloan Kettering Cancer Center, New York, NY, USA.

[12]Department of Pharmacology, Weill Cornell Medicine, New York, NY, USA.

[13]Division of Biostatistics, Department of Population Health Sciences, Weill Cornell Medicine, New York, NY, USA.

[14]Department of Laboratory Medicine, University of California, San Francisco, CA, USA.

[15]Weill Cornell Medicine–Qatar, Doha, Qatar.

[16]Centre for Haemato-Oncology, Barts Cancer Institute, Queen Mary University of London, London, UK.

[17]Caryl and Israel Englander Institute for Precision Medicine and Department of Physiology and Biophysics, Weill Cornell Medicine, New York, NY, USA.

[18]Centre for Lymphoid Cancer, BC Cancer, Vancouver, BC, Canada.

[19]Institute for Biochemistry, Biotechnology and Bioinformatics, Technische Universität Braunschweig, Braunschweig, Germany.

Abstract

INTRODUCTION: Diffuse large B cell lymphomas (DLBCLs) are aggressive malignancies of which ~40% fail to respond or become refractory to treatment. Mechanisms that mediate these poor outcomes are unknown. Most DLBCLs originate from specialized B cells participating in the germinal center (GC) reaction. GCs are transient structures within which antigen-activated B cells undergo proliferative bursting and somatic hypermutation of their immunoglobulin genes to improve affinity against the encountered antigen. High proliferation activity depletes GC B cells of essential biosynthetic precursors. Hence, GC B cells must endure an intense Darwinian competition process, during which they vigorously compete for access to positive selection signals from a limiting number of T follicular helper (T_{FH}) cells. Only few B cells that win this competition receive T_{FH} cell help, which triggers transient expression of the Myc proto-oncogene and biosynthetic growth programs. Unfortunately, GC B cells acquire abundant off-target mutations, making them prone to malignant transformation. Hence, GC B cell selection by T_{FH} cells requires rigorous, but still largely unknown, control mechanisms to prevent unwanted clonal expansion and malignant transformation of abnormal cells.

RATIONALE: Missense mutations of *BTG1* (B cell translocation gene 1) are specific to GC-derived B cell lymphomas, suggesting that their oncogenic function is cell-context specific. *BTG1* mutations help to genetically define a class of DLBCLs that manifest especially poor clinical outcomes and extensive dissemination. This prompted us to explore how *BTG1* mutations contribute to the pathogenesis of these clinically challenging tumors.

RESULTS: We generated mice for the B cell–conditional expression of the most frequent *BTG1* mutation [Gln^{36}→His (Q36H)]. Btg1^{Q36H} cells almost completely outcompeted their wild-type counterparts, specifically in the GC. This competitive fitness manifested as a stronger induction of MYC-dependent growth programs. Wild-type BTG1 associated with many mRNAs, including those for *MYC* and MYC target genes, a function that was significantly lost by BTG1^{Q36H}. Mutant BTG1 expression enhanced *MYC* mRNA loading onto polysomes and induced slightly more-rapid MYC protein induction kinetics and a higher fraction of MYC-positive B cells in murine and human systems. These data suggested a lower threshold for BTG1 mutant cells to respond to T_{FH}-positive selection signals. Accordingly, Btg1 mutant GC B cells experienced faster cell cycle S phase transit and earlier entry into subsequent proliferative bursts. In Bcl2-driven lymphoma mouse models, Btg1^{Q36H} markedly accelerated disease onset, shortened survival, and yielded particularly invasive DLBCL-like lymphomas. Btg1^{Q36H} lymphomas were highly clonal and heavily mutated, reflecting a lymphomagenesis trajectory with increased selection and mutation rounds over time. In patients, *BTG1* mutations scored as strong genetic DLBCL drivers and independently associated with significantly inferior clinical outcomes.

CONCLUSION: Our data suggest that BTG1 serves as a critical gatekeeper controlling a key fitness checkpoint for natural selection of intensely competing B cells during the adaptive immune response. The precise targeting of BTG1 function by missense mutations causes a subtle biochemical impact, whose specific engagement during repetitive rounds of GC B cell positive selection likely explains its substantial oncogenic fitness effect. This reveals the fragility of constraints required to prevent competing B cells from recalling features of uncontrolled natural selection among unicellular organisms and highlights a fine-tuned balance between protection against infection and cancer risk. This effect is reminiscent of the Myc-dependent supercompetition first described during *Drosophila* development. Future therapeutic strategies could potentially take advantage of such evolutionary vulnerabilities to target cancer cell fitness. □

Graphical Abstract

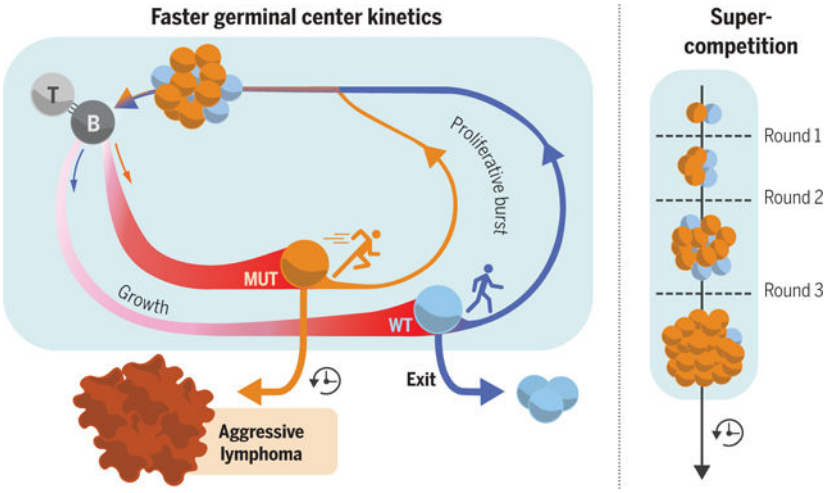

Supercompetition in germinal centers leads to aggressive B cell lymphomas. GC B cells vigorously compete against each other to receive limiting T cell help, which activates MYC-dependent growth programs in preparation for subsequent proliferative bursting. BTG1 mutant GC B cells respond to T cell help signals with faster MYC induction kinetics and more-rapid

entry into the next proliferative phase, which, over many GC rounds, allows them to outcompete wild-type cells, leading to highly fit and disseminated B cell lymphomas.

Abstract

Multicellular life requires altruistic cooperation between cells. The adaptive immune system is a notable exception, wherein germinal center B cells compete vigorously for limiting positive selection signals. Studying primary human lymphomas and developing new mouse models, we found that mutations affecting *BTG1* disrupt a critical immune gatekeeper mechanism that strictly limits B cell fitness during antibody affinity maturation. This mechanism converted germinal center B cells into supercompetitors that rapidly outstrip their normal counterparts. This effect was conferred by a small shift in MYC protein induction kinetics but resulted in aggressive invasive lymphomas, which in humans are linked to dire clinical outcomes. Our findings reveal a delicate evolutionary trade-off between natural selection of B cells to provide immunity and potentially dangerous features that recall the more competitive nature of unicellular organisms.

During the humoral immune response, germinal center (GC) B cells undergo iterative rounds of natural selection to generate high-affinity B cell receptors. This process involves somatic hypermutation and clonal expansion of GC B cells and strictly depends on B cells competing to receive positive selection signals from T follicular helper (T_{FH}) cells (1, 2). T_{FH} cell help allows a few GC B cells to survive and differentiate into memory B cells or plasma cells, or instead undergo additional rounds of proliferative bursting and mutagenesis. Transient induction of Myc- and mammalian target of rapamycin complex 1 (mTORC1)–biosynthetic programs is required to accumulate biomass in preparation for the subsequent proliferative burst (3–5).

The mutagenic and proliferative nature of GC B cells places them at considerable risk for malignant transformation (6, 7). Hence, most immune system neoplasms arise from B cells that have transited the GC reaction. The most common of these are diffuse large B cell lymphomas (DLBCLs), which have classically been separated into germinal center B-like (GCB) and activated B-like (ABC) DLBCLs according to their transcriptional profiles (8). DLBCLs were more recently segregated into genetically defined entities with distinct biological characteristics and mutational profiles (9–11). Among these, the most clinically challenging, MCD/cluster 5, is an ABC-DLBCL subtype featuring extranodal dissemination and high fraction of proliferating cells. Recurrent somatic mutations in *MYD88* and *CD79B* drive proliferation of these lymphomas through chronic activation of Toll-like receptor and B cell receptor signaling, whereas *TBL1XR1* mutations endow them with a post-GC memory B cell phenotype (12, 13). However, the basis for their marked fitness and aggressive phenotypes remains unknown.

Possible clues to these phenotypes may be gleaned from mechanistic deconvolution of other recurrent mutations. For example, somatic missense mutations of *BTG1* (B cell translocation gene 1) occur in up to 70% of MCD-DLBCL cases (11). BTG1 has been reported to regulate gene expression by interacting with transcription factors, mRNA stability regulatory proteins (CNOTs), or the arginine methyltransferase PRMT1 (14–18). Although BTG1 loss results in minor perturbations of early B cell development (19), and a few BTG1

mutants show differential CNOT interaction and tethered-mRNA stability effects in yeast and human embryonic kidney 293T (HEK293T) cells (20), the role of BTG1 in mature B cells and how *BTG1* lymphoma mutations contribute to lymphomagenesis remain unknown. Furthermore, *BTG1* is not deleted in DLBCLs, suggesting that mutations are not simple loss-of-function alleles (11). In this study, we probed the effect of *BTG1* mutation on GC biology and malignant transformation. *BTG1* mutation conferred a supercompetitive phenotype to GC B cells through a discrete acceleration of their response to T_{FH} cell help, resulting in the formation of highly aggressive lymphomas. Our findings illustrate how subtle biochemical perturbations in GC B cells can confer marked competitiveness and oncogenic transformation potential in concert with microenvironmental cues such as T_{FH} cell help.

Results

BTG1 somatic mutations in DLBCLs are genetic drivers

We surveyed the genomic profiles of 25,670 cancer patients, including publicly available DLBCL datasets (9, 21–29). *BTG1* somatic mutations were detected in 11% of DLBCL cases (n = 272/2407), which is frequent given their high genetic heterogeneity, but were rare in other tumor types, suggesting specific BTG1 function in this context (fig. S1A). Within DLBCLs, *BTG1* mutation was enriched in the more clinically unfavorable ABC-DLBCLs (P = 0.0184; fig. S1B), especially those defined as MCD/cluster 5 lymphomas, with 40% of all BTG1 mutant DLBCLs being MCD (fig. S1C). *BTG1* mutations scored among the top DLBCL drivers in a rigorous genetic driver analysis taking into account multiple genomic and epigenomic covariates (Fig. 1A and table S1). Most *BTG1* mutant alleles corresponded to heterozygous missense mutations clustered within the N terminus, which contains several conserved functional motifs (30) (Fig. 1B and table S2). Alpha helix 2 (a2) was most heavily mutated, especially at Gln^{36}, which was most frequently (86%) replaced by a histidine [Gln^{36}→His (Q36H); Fig. 1, B and C, and fig. S1D]. Q36H and additional *BTG1* N-terminal mutations can alter the conformational distribution of BTG1 within the α2–α4 region, as determined by in silico atomistic molecular dynamics simulation (31).

$Btg1^{Q36H}$ generates supercompetitor GC B cells

DLBCLs originate from B cells having transited the GC reaction. To determine the functional impact of *BTG1* mutation during the humoral immune response, we generated a mouse model for conditional expression of mutant Btg1 from the *Rosa26* locus ($R26^{lsl.Btg1Q36H}$), referred to hereafter as Q36H (fig. S2, A to C). We then reverted the Q36H mutation to wild type to generate a wild-type knock-in (WTKI) control line ($R26^{lsl.Btg1wt}$; fig. S2, D to G). Q36H and WTKI mice were crossed to the $Cd19^{Cre}$ strain to induce $Btg1^{Q36H}$ or $Btg1^{WTKI}$ expression in B cells (32). Recombination and expression of Q36H and WTKI alleles was validated in B cells at DNA, RNA, and protein levels (fig. S2, H to M). Notably, the total abundance of *Btg1* transcripts was not increased upon expression of $Btg1^{Q36H}$ or $Btg1^{WTKI}$ from the *Rosa26* locus, indicating an absence of Btg1 dosage effect (fig. S2, J and K). Q36H or WTKI expression in B cells did not perturb early B cell development in the bone marrow nor steady-state mature B cell populations in secondary lymphoid tissues and peritoneal cavity (fig. S3).

To investigate the GC response, we immunized Q36H ($R26^{lsl.Btg1Q36H/+}$; $Cd19^{Cre/+}$), WTKI ($R26^{lsl.Btg1wt/+}$; $Cd19^{Cre/+}$), and CRE-control ($R26^{+/+}$; $Cd19^{Cre/+}$) or CREneg-control ($R26^{lsl.Btg1Q36H/+}$; $Cd19^{+/+}$) mice with sheep red blood cells (SRBCs), a T cell–dependent antigen, and analyzed spleens 10 days later. The GC response to SRBCs remained unchanged in Q36H and WTKI animals (fig. S4). Using a different T cell–dependent antigen [(4-hydroxy-3-nitrophenyl)acetyl (NP) conjugated to ovalbumin (OVA)] to assess antigen-specific responding cells, we further observed no change in Q36H versus CRE mice over the course of the GC reaction (fig. S5).

Most GC-derived lymphoma oncogenes affect GC size, composition, or output. Hence, the absence of such effects in the $Btg1^{Q36H}$ setting was puzzling. However, these aspects do not necessarily reflect possible selective advantages within B cell clones. To directly test competitive fitness of Q36H GC B cells in vivo, we crossed our mice to the B1–8^{hi} allele. B1–8^{hi} encodes a B cell receptor with high NP affinity in B cells with a lambda immunoglobulin light chain (~10 to 15% of murine B cells) that facilitates their entry into GCs upon NP immunization (33). We adoptively transferred a 50:50 ratio of B1–8^{hi}/Q36H (B1–$8^{hi\,+/-}$; $R26^{lsl.Btg1Q36H/+}$; $Cd19^{Cre/+}$; CD45.1/2) and B1–8^{hi}/CREneg-control (B1–$8^{hi\,+/-}$; $R26^{lsl.Btg1Q36H/+}$; $Cd19^{+/+}$; CD45.1) resting B cells into wild-type CD45.2 (non-B1–8^{hi}) recipients (Fig. 2A). Q36H GC B cells showed a progressive competitive advantage over time, reaching up to ~90% of total GC B cells by day 14 (Fig. 2A and fig. S6A). Q36H did not confer a competitive advantage to non-GC B cells (fig. S6A), and the GC fitness gain was not associated with changes in GC polarity (fig. S6B). A similar advantage of B1–8^{hi}/Q36H GC B cells occurred when competing against B1–8^{hi}/CRE-controls instead (B1–$8^{hi\,+/-}$; $R26^{+/+}$; $Cd19^{Cre/+}$; CD45.1; fig. S6C). In contrast, B1–8^{hi}/WTKI cells did not show a competitive advantage in GC B cells over non-GC B cells (fig. S6D). To confirm that the Q36H fitness advantage was not due to the extra $R26^{Btg1}$ copy or $Cd19^{Cre}$ knock-in, we directly placed B1–8^{hi}/Q36H and B1–8^{hi}/WTKI cells in competition. Q36H again outcompeted WTKI cells in the GC compartment, whether gating or not on antigen-specific (lambda^{+}NP^{+}) cells and even given a lower Q36H abundance in the starting NB or non-GC B compartment (Fig. 2B and fig. S7A). To assess Q36H GC B cell fitness in the context of a polyclonal immune response (without B1–8^{hi}–engineered antigen specificity), we transferred resting B cells from Q36H, WTKI, or CRE-controls into wild-type recipients and measured GC contribution of each genotype versus recipient cells. Q36H cells showed greater expansion within the GC compartment (18% average) as compared with WTKI and CRE at day 21 (~5%; Fig. 2C). Such expansion was similar in NP-specific GC B cells and did not occur in the NB compartment (fig. S7, B and C). In these experiments, $Cd19^{Cre}$-mediated recombination efficiency was as expected (32), and the Q36H GC B cell advantage was accompanied by a measurable and significant enrichment of Q36H recombined alleles in GC B versus NB cells (fig. S7D). We next assessed proliferation in competing Q36H and CRE B cells in T cell–independent B cell activation by NP-Ficoll immunization. We observed similar proportion and carboxyfluorescein succinimidyl ester (CFSE) proliferation dye dilution of antigen-specific (lambda^{+}NP^{+}) Q36H and CRE B cells over time (fig. S7E). Thus, $Btg1^{Q36H}$ provided a competitive fitness advantage specifically to GC B cells during T cell–dependent immune responses, independently of antigen affinity. Given the lack of

GC-specific phenotype in mice expressing $Btg1^{WTKI}$ in B cells, we focused subsequent functional experiments on mice expressing $Btg1^{Q36H}$.

$Btg1^{Q36H}$ induces MYC-associated biosynthetic programs in GC B cells

To gain insight into the competitive advantage conferred by mutant Btg1, we next performed RNA sequencing (RNA-seq) in Q36H and CRE-control GC B cells (fig. S8A). As noted earlier, total abundance of *Btg1* transcripts was similar in both groups (fig. S8B). Only ~15% of Btg1 transcripts carried the Q36H mutation (fig. S8C), which is comparable to the fraction of mutant BTG1 transcripts (17 to 45%) in $BTG1^{Q36H}$ DLBCL patients (n = 6; fig. S8D). We detected no significant differences in gene expression profiles using both unsupervised and supervised analyses, except for the expected reduction in *Rosa26* due to the knock-in (fig. S8, E and F). Bulk RNA-seq represents a composite of heterogeneous GC B cells in their various transitional states, which could mask effects occurring in subpopulations of cells. We therefore performed gene set enrichment analysis (GSEA) using MSigDB Hallmark and Canonical Pathway gene set collections (34–36) to determine whether we could detect subtler transcriptional perturbation in groups of coordinately regulated genes. We identified positive enrichment of 94 signatures [false discovery rate (FDR) < 0.05], most of them related to activation of biosynthetic pathways, mitochondrial function, and MYC target genes (Fig. 3A and table S3). A network connectivity analysis revealed that MYC targets were among the highest connected signatures, suggesting a central role for MYC (Fig. 3A).

Myc is induced transiently together with mTORC1 activation upon receiving strong T_{FH} cell help during selection in the anatomically defined GC light zone (LZ) (3–5). Myc and mTORC1 biosynthetic programs trigger GC B cell growth, a prerequisite for their subsequent clonal expansion in the GC dark zone (DZ). Accordingly, we observed significant enrichment for signatures induced by T_{FH} cell help in LZ-to-DZ recycling GC B cells, as well as MYC and mTORC1 programs in Q36H versus CRE (Fig. 3B and table S4). The same signatures were significantly enriched among human BTG1 mutant DLBCL patients as compared with BTG wild-type DLBCLs in two independent cohorts (excluding BTG2 mutant patients; Fig. 3B and fig. S8G). Among ABC-DLBCLs, BTG1 mutant cases also showed higher expression of these signatures (fig. S8H). For functional studies, we generated isogenic human DLBCL cells with ectopic and equivalent expression of $BTG1^{Q36H}$ versus $BTG1^{WT}$ (fig. S8, I and J). In this model, $BTG1^{Q36H}$ expression yielded a similar enrichment of LZ-to-DZ recycling, MYC, and mTORC1 signatures (fig. S8K). Furthermore, genes differentially induced [fold change (FC) > 1.5; FDR < 0.01; table S4] in $BTG1^{Q36H}$ versus $BTG1^{WT}$ DLBCL cells were significantly and exclusively enriched for MYC and MAX DNA binding motifs (fig. S8L). The corresponding $BTG1^{Q36H}$ signature was also significantly enriched in BTG1 mutant DLBCL patients (FDR < 0.001; fig. S8M), indicating consistency of BTG1 mutant effects between murine GC and human DLBCL cases. In line with enhanced biosynthetic rates, $Btg1^{Q36H}$ GC B and $BTG1^{Q36H}$ DLBCL cells showed increased RNA content and cell size (Fig. 3, C and D, and fig. S8, N and O). These data suggested that *BTG1* mutation enhances biosynthetic fitness programs normally associated with positive selection and Myc/mTORC1 activation during the GC reaction, an effect that is maintained in established DLBCLs.

MYC-related signatures could be enriched because of either higher expression of Myc or expansion of Myc-positive (Myc^{+}) GC B cells. To address this question, we crossed our Q36H mice to the Myc^{GFP} reporter line, in which endogenous Myc protein is fused to green fluorescent protein (GFP) (37). To better focus our analysis on GC B cells, we used the $C\gamma 1^{Cre}$ line (38) to drive $Btg1^{Q36H}$ expression (Fig. 3E). The proportion of Myc^{GFP+} GC B cells was significantly higher in Q36H versus CRE-control mice (Fig. 3F), yet Myc^{GFP+} cells in Q36H and CRE mice manifested similar Myc^{GFP} protein and *Myc* transcript levels (fig. S8, P and Q). As expected, RNA-seq analysis on Myc^{GFP+} versus Myc^{GFP-} GC B cells showed strong enrichment of the LZ-to-DZ recycling, MYC, and mTORC1 signatures in both Q36H and CRE (fig. S8R). However, comparing Myc^{GFP+} versus Myc^{GFP-} cells from Q36H versus CRE mice revealed up-regulation of 201 transcripts in Q36H Myc^{GFP+} (Fig. 3G and table S4). These genes were significantly enriched for Myc immediate early direct target genes (39), as well as genes activated by T_{FH} cell help through cytokine signaling (Fig. 3H). Thus, the fitness advantage of Btg1 mutant GC B cells was linked to increased proportion of Myc-expressing cells and enhanced activation of early Myc programs, without alteration of steady-state Myc expression levels per cell.

Q36H impairs BTG1 association with MYC and other transcripts involved in LZ-to-DZ recycling

We next explored how $BTG1^{Q36H}$ specifically influences MYC expression and T_{FH} cell help–related transcriptional programs. The BTG1 family proteins TOB1 and TOB2, which share the conserved N-terminal domain with BTG1, were recently shown to interact with RNAs (40). We thus performed RNA immunoprecipitation (RIP) assays using V5-tagged $BTG1^{WT}$, $BTG1^{Q36H}$, or enhanced GFP (EGFP) proteins as baits in our DLBCL cells (fig. S9A). As compared with EGFP negative control, $BTG1^{WT}$ enriched ~3000 unique mRNA species, whereas $BTG1^{Q36H}$ enriched only ~700 (fig. S9B). This effect was largely due to loss of $BTG1^{WT}$-associated mRNAs (fig. S9C). Significantly reduced pull-down with $BTG1^{Q36H}$-V5 versus $BTG1^{WT}$-V5 was observed for 732 transcripts, which notably included the *MYC* mRNA (log2FC > 2, $q < 0.05$; Fig. 4A and table S5). These transcripts were highly enriched for LZ-to-DZ recycling and Myc^{GFP+} signatures and marginally enriched for the centrocyte signature (which includes the small Myc^{+} population), but not for other GC or post-GC subpopulations (Fig. 4B). We further validated $BTG1^{WT}$-*MYC* mRNA association and reduced enrichment with $BTG1^{Q36H}$ in independent RIP experiments by quantitative polymerase chain reaction (qPCR; Fig. 4C). We next tested whether BTG1 directly binds RNA by ultraviolet (UV) cross-linking and immunoprecipitation (CLIP) of RNAs interacting with V5-tagged $BTG1^{WT}$, $BTG1^{Q36H}$, and EGFP as compared with canonical RNA-binding proteins Musashi-2 (MSI2) and human antigen R (HuR). No RNA was enriched with EGFP, and very little RNA and no enrichment for RNA-protein complexes right above the expected size of V5-tagged $BTG1^{WT}$ or $BTG1^{Q36H}$ was observed, as opposed to MSI2 and HuR (fig. S9D).

These data suggested that $BTG1^{WT}$ indirectly associates with transcripts involved in T_{FH} cell help and MYC programs to attenuate their expression, a function that is lost by BTG1 lymphoma mutants. In line with this, expressing $BTG1^{WT}$ in our isogenic DLBCL cells resulted in depletion of the LZ-to-DZ recycling, MYC, and mTORC1 signatures (fig. S9E)

and reduced cellular RNA abundance, as compared with vector-control cells (fig. S9F). We categorized differentially expressed genes according to their behavior in $BTG1^{WT}$ and $BTG1^{Q36H}$ DLBCL cells. Many transcripts were regulated in a similar fashion (fig. S9G). However, genes repressed by $BTG1^{WT}$ but not $BTG1^{Q36H}$ were largely restricted to the LZ-to-DZ recycling, MYC, and mTORC1 signatures, and complementarily, genes induced by $BTG1^{WT}$ but not $BTG1^{Q36H}$ were mostly enriched for MYC-repressed and anti-mTORC1 signatures (fig. S9G and table S6). Hence, wild-type BTG1 normally associates with *MYC* and transcripts relevant to LZ-to-DZ recycling GC B cells, an effect that is impaired by mutational disruption of its N-terminal domain.

$BTG1^{Q36H}$ lowers the threshold for MYC protein synthesis

We wondered whether loss of *MYC* mRNA association upon BTG1 mutation might alter MYC protein induction kinetics, perhaps enabling cells to reach high MYC plateau levels more rapidly and yielding the observed increased fraction of MYC^{+} cells. BTG1 can regulate mRNA stability in T cells (41). However, *MYC* mRNA half-life was comparable in $BTG1^{Q36H}$ and $BTG1^{WT}$ DLBCL cells exposed to transcription inhibitor actinomycin D (fig. S10A). To investigate MYC protein expression kinetics, we placed $BTG1^{Q36H}$ and $BTG1^{WT}$ isogenic DLBCL cells under serum deprivation and performed Western blots for MYC and BTG1 (by means of the V5 tag) at serial time points between 15 min and 2 hours after re-feeding (fig. S10B). MYC was induced >1.5-fold between 15 and 30 min in $BTG1^{Q36H}$ but did not change significantly in $BTG1^{WT}$-expressing cells (fig. S10B). *MYC* mRNA abundance remained unchanged under similar conditions (fig. S10C). To further investigate the increased MYC protein levels, we treated our DLBCL cells with cycloheximide (CHX) to inhibit protein synthesis, which revealed no effect of $BTG1^{Q36H}$ on MYC protein stability (fig. S10D). We then performed an MG132 treatment time course to inhibit protein degradation. This showed an earlier and higher accumulation of MYC protein levels in $BTG1^{Q36H}$ cells (a 4.5-fold peak at 2 hours MG132 versus dimethyl sulfoxide (DMSO) in $BTG1^{Q36H}$ cells compared with a 3.8-fold peak at 4 hours MG132 versus DMSO in $BTG1^{WT}$ cells; fig. S10E). Both $BTG1^{WT}$ and $BTG1^{Q36H}$ protein levels decreased upon reaching high MYC protein levels, consistent with reports that Myc can down-regulate Btg1 (42) (fig. S10E). Accordingly, *Btg1* mRNA levels were reduced in Myc^{GFP+} versus Myc^{GFP-} GC B cells (fig. S10F). To measure MYC protein levels per cell, we performed MYC flow cytometry analyses in similar MG132 time courses. The fraction of MYC^{+} cells was larger (~1.5-fold) in $BTG1^{Q36H}$ cells than in $BTG1^{WT}$ cells throughout the time course and was accompanied by a mild and faster up-regulation of MYC protein abundance in MYC^{+} cells (Fig. 4D and fig. S11A). *MYC* mRNA levels remained comparable between $BTG1^{Q36H}$ and $BTG1^{WT}$ cells (fig. S11B). These observations suggest that $BTG1^{Q36H}$ lowered the threshold for MYC protein synthesis, resulting in a greater fraction of cells expressing MYC. Three additional DLBCL-recurrent BTG1 mutants (S43N, A49T, and T39I) accelerated MYC protein induction in a similar fashion (fig. S11C), and this effect was also observed when we expressed $BTG1^{Q36H}$ versus $BTG1^{WT}$ in freshly immortalized primary human GC B cells (43) (fig. S11, D to G).

To directly measure *MYC* mRNA engagement with the translational machinery, we carried out polysome profiling in our isogenic $BTG1^{WT}$ and $BTG1^{Q36H}$ DLBCL cells. We

confirmed that polysomal fractions were enriched for ribosomal proteins (e.g., RPS3; fig. S12A). BTG1^{Q36H} cells showed higher RNA abundance in polysomal fractions as compared with BTG1^{WT} cells, indicative of increased overall translation (Fig. 4E and quantification in Fig. 4F). BTG1^{Q36H} cells also contained a significantly greater abundance of *MYC* transcripts within polysomal fractions (Fig. 4G and fig. S12B). Collectively, these data suggested that wild-type BTG1 association with *MYC* mRNA may restrict MYC translation, an effect that is specifically disrupted by *BTG1* mutations. We hypothesized that this might reduce the threshold for T_{FH} cell help–dependent MYC induction, thereby enhancing the response of GC B cells to T_{FH} cell help signals.

More-rapid S phase completion and DZ commitment by Btg1^{Q36H} LZ-to-DZ recycling cells

The degree of T_{FH} cell help, and therefore Myc induction, determines the ability and speed of GC B cells to transit through S phase and subsequently undergo proliferative burst in the DZ (44, 45). Hence, we predicted that enhanced Myc kinetics due to *Btg1* mutation would enable GC B cells to more efficiently progress through S phase and into the DZ proliferative program. To evaluate whether and how such effects might manifest in the heterogeneous GC milieu, we performed targeted single-cell RNA-seq (n = 496 immune-related genes; table S7) on competing B1–8^{hi}/Btg1^{Q36H} and B1–8^{hi}/CREneg control GC B cells sorted at day 10 after NP immunization, when Q36H cells outcompete control cells by ~70 to 30% (Fig. 5A and fig. S6A). A general overview (2982 cells across three biological replicates) revealed a similar general distribution of individual cell gene expression profiles, without bias toward genotype or biological replicate (fig. S13, A and B). Individual cells were assigned to specific GC B cell subpopulations (DZ, LZ, or LZ-to-DZ recycling) according to their distinctive signatures and marker transcript levels (Fig. 5B).

LZ-to-DZ recycling cells enter S phase but generally do not engage G2/M until transiting into the DZ and expressing the corresponding centroblast (CB) transcriptional program (44). Accordingly, S and G2/M phase signatures were mostly confined to the DZ compartment (fig. S13C). To compare cell cycle progression of Q36H versus control GC B cells, we plotted their frequency according to cell cycle program expression, across a pseudotime scale starting from G1 phase (Fig. 5C). We found a significant increase in Btg1^{Q36H} cell density from S phase entry and throughout G2/M (P = 0.0071; Fig. 5C). As expected, cells expressing the LZ-to-DZ recycling program localized at the G1-to-S transition and extended into G2/M along this pseudotime axis (pseudotime units 9 to 14; Fig. 5D). We then projected the DZ and G2/M signatures onto the same axis. GC B cells at the LZ-to-DZ recycling pseudotime transition showed earlier induction and greater proportion of Btg1^{Q36H} cells having initiated DZ (P = 0.0117; Fig. 5E) and G2/M (P = 0.0202; Fig. 5F) programs. Along these lines, we identified 28 genes with differential expression in Btg1^{Q36H} versus control cells, which mainly corresponded to changes in the proportion of cells expressing these genes (chi-square $P < 0.05$) and with most genes being related to cell cycle and lymphoma (fig. S13D). Therefore, Btg1^{Q36H} LZ-to-DZ recycling GC B cells engaged the proliferative DZ program earlier and in greater proportions.

These single-cell profiles raised the question of whether Btg1 mutant GC B cells may complete S phase more rapidly or at a higher rate. To explore this, we measured cell

cycle kinetics in competition experiments. To distinguish between entry, mid-late, and post S phase cells, we injected 5-ethynyl-2′-deoxyuridine (EdU) and 5-bromo-2′-deoxyuridine (BrdU) at 1.5 hours and 0.5 hours before euthanasia, respectively (46) (Fig. 5G). We validated the expected advantage of Btg1^{Q36H} GC B cells under these conditions, with no change in DZ:LZ polarity nor advantage among non-GC B cells (fig. S13, E and F). We observed no difference in S phase entry (BrdU^{+} only) in either centrocyte (CC) or centroblast (CB) populations (Fig. 5G). In contrast, there was a significant increase in Btg1^{Q36H} CC and CB progressing through mid-late S phase (BrdU^{+}EdU^{+}) and in Btg1^{Q36H} CB post S phase (EdU^{+} only; Fig. 5G). These observations suggested that Btg1 mutant GC B cells transited and completed S phase more rapidly than control cells. To distinguish whether such effects were specific to the LZ-to-DZ recycling GC B cells, we next performed in vivo Edu incorporation assays in our Q36H/*Cg1*^{Cre}/*Myc*^{GFP} mice to detect S phase–experienced cells in Myc^{GFP+} versus Myc^{GFP-} GC B populations. To avoid losing the small number of Myc^{GFP+} GC B cells during EdU staining, sorted cells were fixed and stained by immunofluorescence on slides (Fig. 5H and fig. S13G). A significantly higher proportion of EdU^{+} cells was detected in Q36H versus CRE Myc^{GFP+} GC B cells ($P = 0.0304$; Fig. 5H), whereas there was no change in Q36H versus CRE Myc^{GFP-} cells. This suggested that Btg1^{Q36H} induced an S phase transit advantage specifically to LZ-to-DZ recycling GC B cells.

Competitive advantage conferred by Btg1^{Q36H} links to faster LZ-DZ kinetics

Our data so far suggest that *Btg1* mutation provides a GC fitness advantage by reducing the threshold to T_{FH} cell help response, as manifested by facilitated Myc protein induction, DZ program commitment, and S phase completion. To determine whether these changes could explain the Btg1^{Q36H} fitness advantage, we used established in silico mathematical models that reflect different aspects of GC temporal and clonal selection dynamics, including B cell receptor and CD40 signaling, antigen uptake, and Myc and mTORC1 induction (47). Comparing multiple different combinatorial perturbations of these signals, we found that providing GC B cells with a modest increase in the speed of T_{FH} cell help response, corresponding to a 1.12-fold increase in the rate of Myc induction and mTORC1 activation, recapitulated the Btg1^{Q36H} competitive advantage observed in vivo (fig. S14A). However, under noncompetitive conditions, this model predicted higher GC and CB proportions for Btg1 mutant (fig. S14A), two features that were not observed in vivo (see figs. S4 and S5). Taking into account our observation of a more rapid S phase completion, we determined that shortening the S phase by 21%, in addition to providing 1.12-fold faster T_{FH} cell help response, recapitulated the competitive advantage of Btg1^{Q36H} GC B cells without altering GC volume and polarity under noncompetitive conditions, more accurately reflecting the Btg1^{Q36H} in vivo phenotypes (fig. S14B). These parameters further predicted that Btg1 mutant GC B cells would undergo an increased number of GC rounds over the course of the GC reaction ($P < 2 \times 10^{-16}$ at day 10; Fig. 6A).

To test this scenario functionally, we synchronized competing Q36H and WT GC B cells receiving targeted T_{FH} cell help in vivo and tracked their LZ-to-DZ kinetics. T cell help can be elicited by injecting an OVA-conjugated anti-DEC205 antibody (αDEC205-OVA), which binds to the B cell surface receptor DEC205 and delivers OVA to the

major histocompatibility complex class II (MHC-II) presentation pathway, inducing strong interactions with OVA-specific T_{FH} cells (44) (Fig. 6B). We adoptively transferred 3% Q36H (B1–$8^{hi+/-}$; *DEC205*$^{+/+}$; *R26*$^{sl.Btg1Q36H/+}$; *Cd19*$^{Cre/+}$; CD45.1) and 7% WT (fluorescent B1–$8^{hi+/-}$; *DEC205*$^{+/+}$; CD45.1) resting B cells, to reach a 50:50 proportion of Q36H and WT cells at 6 to 7 days into the GC reaction. The remaining 90% were B1–$8^{hi+/-}$; *DEC205*$^{-/-}$; CD45.1/2 cells that lack the DEC205 receptor and do not receive targeted T_{FH} cell help, to better reflect physiological conditions where T_{FH} cell help is only available to a small fraction of GC B cells (Fig. 6C). In this three-way competition system, the different transferred cell populations were distinguished using a combination of congenic and fluorescent markers. Recipient CD45.2 mice were primed with OVA before the B cell transfer to generate OVA-specific T_{FH} cells. The day after transfer, mice were boosted with NP-OVA to recruit OVA-specific recipient T_{FH} cells and NP-specific B1–8^{hi} transferred B cells into the GC reaction.

We delivered T_{FH} cell help to competing DEC205$^{+/+}$ Q36H and WT cells 6 to 7 days into the GC reaction by injecting αDEC-OVA. We then measured the proportion of GC B cells in LZ (CC) and DZ (CB) over time (0, 36, 48, and 72 hours) after T_{FH} cell help delivery (Fig. 6, C and D). In line with previous work (44), DEC205$^{-/-}$ cells remained enriched in the LZ over this time course, showing a stable DZ:LZ ratio, and did not expand after anti-DEC205-OVA injection, whereas DEC205$^{+/+}$ cells moved to the DZ (as CB) and expanded between 48 and 72 hours (Fig. 6, D and E, and fig. S14, C and D). Within DEC205$^{+/+}$ cells, T_{FH} cell help induced a more robust increase in DZ:LZ ratio for Q36H GC B cells as compared with WT, peaking at 48 hours ($P = 0.0187$; Fig. 6E and fig. S14D). These results reflected a greater DZ reentry for Btg1^{Q36H} GC B cells upon receiving T_{FH} cell help signals. Collectively, these data suggested that subtle acceleration of T_{FH} cell help–related Myc induction and S phase completion led to a progressive and marked fitness advantage of GC B cells, by conferring greater DZ reentry potential and an opportunity to undergo increased GC repetitive rounds (Fig. 6F).

Btg1^{Q36H} expression induces highly aggressive and rapidly progressive lymphomas

We next explored whether *Btg1*^{Q36H} is a bona fide lymphoma oncogene. Given that MCD/cluster 5 DLBCLs derive from B cells having transited the GC reaction, we induced Btg1^{Q36H} expression using *Cγ1*^{Cre}. MCD-DLBCLs typically express high BCL2 levels (11). We crossed our mice to the VavP-*Bcl2* lymphoma mouse model (48, 49) to reflect this biology. We generated cohorts of Bcl2, Bcl2+Q36H, Q36H, CREneg, and CRE mice through bone marrow hematopoietic stem cell transplantation into syngeneic wild-type recipients (Fig. 7A). Bcl2+Q36H animals displayed shorter survival than did Bcl2 animals ($P = 0.0005$; Fig. 7B). Notably, survival outcomes were indistinguishable between Q36H-only mice and CREneg or CRE control groups ($P > 0.47$; Fig. 7B). As opposed to Bcl2+Q36H, Bcl2+WTKI animals did not experience more-rapid mortality rates than Bcl2 animals, in a similar transplantation cohort using fetal liver hematopoietic stem cells (fig. S15, A to C).

To determine whether mutant Btg1 accelerated disease onset, we analyzed a subset of seemingly healthy Bcl2+Q36H and Bcl2 animals ($n = 5$ per group) at 8 months after

transplantation. Bcl2+Q36H mice manifested increased splenomegaly ($P = 0.0257$; Fig. 7C and fig. S15D). Histologically, Bcl2 spleens showed a prominent follicular pattern but otherwise largely intact architecture, whereas Bcl2+Q36H animals manifested distortion and expansion of B cell follicles ($B220^+$) and GC areas (PNA^+; Fig. 7D). GC B cells (FAS^+CD38^-) were increased in proportion to B cells ($B220^+$; fig. S15E), were larger (fig. S15F), contained a higher fraction of mTORC1-activated cells [phosphorylated S6 ($pS6^+$); fig. S15G], and were more clonal (IgVH PCR on cDNA; fig. S15H) in Bcl2+Q36H versus Bcl2 spleens. Unsupervised analysis of RNA-seq performed in these lymphoma cells showed markedly distinct transcriptional profiles (fig. S15I). Mutant BTG1-induced signatures such as positively selected GC B cells and MYC targets were significantly enriched (FDR < 0.001 and 0.005, respectively), suggesting maintenance of BTG1 mutant effects (fig. S15J). Lymph node architecture was severely disrupted in Bcl2+Q36H mice, with expansion of extrafollicular areas containing enlarged and proliferative ($Ki67^+$) lymphoma cells, as compared with Bcl2 (Fig. 7E). Most notably, Bcl2+Q36H mice displayed invasion of malignant B cells into extranodal tissues such as the liver, kidney, and lung, whereas Bcl2 mice only manifested minor perivascular infiltrates in these tissues (Fig. 7F and fig. S15K).

To assess $Btg1^{Q36H}$ effect on the genetic trajectory during lymphomagenesis, we performed B cell receptor (BCR) sequencing (fig. S16, A and B). All lymphomas harbored somatic hypermutation activity, typical of their GC origin (fig. S16C). Bcl2+Q36H lymphoma B cells manifested significantly greater mutational burden (fig. S16D) and clonal expansion when compared with Bcl2, as represented by their lower Simpson's index and expanded phylogenetic trees (Fig. 7G and fig. S16, E and F). Furthermore, Bcl2+Q36H clonal lineages presented lower estimated replacement-to-silent mutation rate ratios (dN/dS) than Bcl2, which is indicative of purifying selection and consistent with more cycles of division and mutation in germinal centers (50) (fig. S16G). In line with this, mathematical modeling (fig. S14B) predicted a higher number of divisions in selected mutant versus wild-type GC B cells over the course of the GC reaction (fig. S16H). Collectively, lymphoid architecture disruption and invasion of extralymphoid tissues by more proliferative, dysplastic, highly mutated, and clonally expanded tumor cells indicated more advanced and phenotypically malignant disease in Bcl2+Q36H mice, with the genetics indicating that $Btg1^{Q36H}$ B cells underwent more rounds of selection and somatic hypermutation, in line with their fitness advantage.

Further along these lines, moribund Bcl2 mice presented with low-grade follicular centrocyte-like lymphoma patterns, whereas moribund Bcl2+Q36H mice featured sheets of larger lymphoid cells, reminiscent of DLBCL with many cells showing immunoblastic or plasmacytoid appearance (Fig. 7H). These differential features were observed in the spleen, as well as extranodal tissues (Fig. 7H). Bcl2+Q36H mice also uniquely manifested cases of extreme disease invasiveness into peripheral organs (fig. S16I), underlining the impact of $Btg1^{Q36H}$ in driving phenotypically high-grade aggressive lymphomas, with features similar to human cases.

Consistent with these aggressive phenotypes, we observed inferior clinical outcomes for *BTG1* mutant patients within ABC-DLBCLs from publicly available cohorts (9, 23, 24)

(P = 0.0011; Fig. 7I). Univariable Cox regression further showed significant association between *BTG1* mutational status and inferior overall survival among ABC-DLBCLs (P = 0.0013; Fig. 7J and fig. S16J). Notably, a multivariable Cox regression analysis, including DLBCL genetic subtype (LymphGen), gender, International Prognostic Index (IPI), and *BTG1* mutation status as covariates, showed that *BTG1* mutation remained significantly associated with overall survival (P = 0.0190; Fig. 7J and fig. S16J). Collectively, these data indicated that *BTG1* mutation presents potent oncogenic properties. Consistent with its role in providing supercompetitive fitness to GC B cells, mutant BTG1 conferred an aggressive and tissue-invasive phenotype to B cell lymphomas, resulting in extranodal spread and inferior clinical outcomes.

Discussion

Multicellular life requires individual cells to sacrifice competitive fitness to ensure homeostasis and survival. Mechanisms that enable “altruistic” cooperation between cells include restraining cell proliferation and preventing acquisition of somatic mutations among other functions and are often viewed as weakened in cancer (51). However, certain nonaltruistic, competitive processes take place in normal embryonic development (52). The archetypal example of supercompetition was first described during *Drosophila* development, whereby cells with greater Myc expression outgrow and may also cull neighbor cells with slightly lower Myc levels (53, 54). The GC reaction provides an intriguing microcosm of the cancer “return to unicellularity” concept in normal nonembryonic physiology, whereby restraints on proliferation and somatic mutations are attenuated and a Myc-dependent competitive process of clonal diversification and selection takes place. Critical to keeping this process under control, expression of Myc is permitted only transiently in GC B cells, together with mTORC1 activation, to provide time-limited biosynthetic capabilities (5).

The absolute arbiter of Myc induction in GC B cells is the intensity of T_{FH} cell help signals received on the basis of affinity for cognate antigen. The resulting range of Myc “doses” can determine initial S phase duration and how many divisions a selected GC B cell undergoes (45, 55). Our findings suggest that in addition to Myc dosage, the rate of Myc protein induction may influence GC B cell fitness, because it is associated with earlier S phase completion, greater DZ reentry, and earlier activation of proliferative programs. Naïve B cell activation models also suggest a critical function for Myc induction kinetics in determining B cell expansion and cell fate (56). However, the competitive gain conferred by mutant Btg1 was restricted to the GC B cell compartment. Thus, analogous to embryonic supercompetition, GC B cells with slightly superior Myc induction kinetics have the potential to outcompete and dominate the GC reaction through clonal expansion.

Given these scenarios, it is plausible that B cells would have evolved ways to control immune signaling thresholds for Myc induction, especially because GC B cells are exposed to an environment rich in growth-promoting cytokines and ligands. Our data suggest that wild-type BTG1-mediated restriction of MYC translation may represent one such mechanism, acting as a safeguard or gatekeeper against unrestrained “unicellular-like” fitness. Mutant BTG1 released MYC from this restrictive effect, thus converting GC B cells into supercompetitors that transformed into extremely aggressive lymphoma cells.

Moreover, Btg1 mutant cells aberrantly retained MYC signatures while activating DZ and G2/M programs, suggesting that biosynthetic growth and proliferation abnormally coexisted rather than being strictly separated. Future studies will determine whether this supercompetition effect is further associated with eliminating wild-type cells, perhaps depriving them from positive selection signals or resource utilization in their microenvironment. The impact of BTG1 mutation on the magnitude of T_{FH} cell help response and MYC induction kinetics was quite subtle, implying that competing GC B cells operate at the most extreme limits of multicellular homeostasis, a small perturbation of which is sufficient to tip the balance toward malignancy. The iterative nature of the GC reaction may further amplify this subtle effect over time. These findings suggest a delicate evolutionary trade-off between defending vertebrate organisms from infections versus facilitating certain “atavistic” features in B cells that recall the more intense and dynamic features of unicellular life.

In T cells, BTG1 was reported to maintain quiescence through global mRNA degradation (41) and interaction with CCR4-NOT (15, 20, 57), a deadenylase complex regulating mRNA stability. In HEK293T cells, certain BTG1 lymphoma mutants manifested impaired interaction with CCR4-NOT (20). However, mutant BTG1 did not affect *MYC* mRNA levels or mRNA stability in GC or DLBCL cells. The BTG family member TOB1 potentially binds mRNAs through 3′ untranslated region (3′UTR), 5′UTR, and coding sequences, suggesting functions beyond mRNA stability regulation (40). However, BTG1 lacks TOB1 C-terminal domain or any known RNA binding domain and instead associated with RNAs indirectly. Given that BTG1 mutants facilitated translation of MYC and potentially other proteins, we hypothesize that wild-type BTG1 association with *MYC* mRNAs restricts MYC translation, until reaching a critical T_{FH} cell help strength threshold, whereas mutant BTG1 lowers this threshold through impaired association with *MYC* mRNAs. These effects are likely mediated through interaction with as of yet unknown RNA binding proteins that might be destabilized by the altered protein conformation induced by mutations such as Q36H (31). This would confer a partial dominant-negative effect, whereby mutant BTG1 could occupy wild-type BTG1 space, preventing its ability to form functional RNA regulatory complexes while preserving other BTG1 functions. The dominant effect of these mutations is further underlined by the relatively low fraction of *BTG1* mutant transcripts in primary human DLBCLs and our animal models. Although *BTG1* is described as a putative tumor suppressor gene in several cancer types (58), it behaved instead as a proto-oncogene in DLBCL. This is indicated by its functional gain-of-fitness effects and focal mutational pattern, but only rare truncating mutations or loss of heterozygosity. Other genes can act both as tumor suppressors and proto-oncogenes depending on the cellular context (59, 60). For example, the poly-comb protein EZH2 is a tumor suppressor deleted in leukemia, as is *BTG1* (61), but is an oncogene with gain-of-function mutations in B cell lymphoma (6).

Myc can suppress Btg1 expression through induction of *miR-17–92* (42), suggesting a positive feedback mechanism. Indeed, we observed that BTG1 expression was reduced in Myc-positive GC B cells or upon induction of MYC in DLBCL cells, and *miR-17–92* deficiency impairs GC responses (62). In line with antagonistic effects, *MYC* and *BTG1* mRNA levels are inversely correlated during cell cycle progression in stimulated peripheral blood lymphocytes and NIH3T3 cells (63). However, there may be additional mechanisms

through which MYC can repress BTG1 expression, given that in our DLBCL cells, V5-tagged BTG1 lacked the 3′UTR binding sites for *miR-17–92*. *Btg1* transcript levels are evidently tightly controlled in GC B cells because expression of $Btg1^{Q36H}$ or $Btg1^{WT}$ from the *Rosa26* locus did not affect overall *Btg1* transcript abundance.

Finally, the lymphomagenic potential of mutant BTG1–induced fitness was underlined by its powerful cooperative effect with BCL2 overexpression, both of which are associated with the MCD-DLBCL subtype. The competitive advantage conferred by mutant BTG1 might be especially deleterious in cells with constitutive Toll-like receptor and B cell receptor signaling due to *MYD88* and *CD79B* mutations. Alternatively, the aberrant memory and clonal precursor cells induced by *MYD88* and *TBL1XR1* mutations (12, 13, 64) could gain potential fitness advantage for reentry into subsequent GC reactions. Finally, the supercompetitor phenotype conferred by *BTG1* mutations seems to manifest clinically, because *BTG1* mutation independently associated with inferior outcome among ABC-DLBCLs. It is thus warranted for future studies to explore potential therapeutic vulnerabilities that could be exploited for treatment of these lethal tumors.

Potential limitations

The lymphomagenic potential of $Btg1^{Q36H}$ or $Btg1^{WT}$ was evaluated in separate experiments without affecting our conclusions, because they were evaluated in comparison to their respective positive and negative controls in each experiment (Fig. 7B and fig. S15B) in comparable experimental setups (fig. S15C). In some mouse experiments, we assessed mutant $Btg1^{Q36H}$ effects using animals that did not carry the $Cd19^{Cre}$ allele. This is not expected to be an issue for the following reasons: (i) We observed a gain-of-function phenotype (i.e., gain of competitiveness) rather than a loss-of-function effect, and Cre-associated toxicity would, on the contrary, impair GC B cell competitiveness through cell-killing effects (65). (ii) Cre knock-in at the *Cd19* locus results in only one functional *Cd19* allele (32). Given its function as a BCR co-receptor, $Cd19^{Cre}$ knock-in would be expected to reduce B cell activation and competitiveness. (iii) Throughout the manuscript, and using multiple orthogonal approaches, Q36H was shown to provide a similar competitive advantage to GC B cells against any tested control, including Cre-positive and Cre-negative cells (e.g., Fig. 2, A to C, and figs. S6, A and C, S7, A and B, and S13E).

Materials and methods

Mouse models

Animal care was in strict compliance with institutional guidelines established by Weill Cornell Medicine, *Guide for the Care and Use of Laboratory Animals* (66), and the Association for Assessment and Accreditation of Laboratory Animal Care International. All mouse procedures were approved by the Research Animal Resource Center and Institutional Animal Care and Use Committee of Weill Cornell Medicine (protocol #2011–0031). All mouse experiments were conducted using age- and sex-matched animals 8 to 14 weeks old, unless specified otherwise. All experiments included male and female animals in all groups, except for adoptive transfers, with all recipient mice being males. No sex-based influence or bias was detected in the observations made in this work.

Conditional knock-in Btg1^{Q36H} mice (*R26*$^{lsl.Btg1Q36H}$) were generated by ingenious Targeting Laboratory Inc. (Ronkonkoma, NY, USA) via insertion of a stop cassette in intron 1 of the *Rosa26* locus followed immediately by a mutated murine *Btg1*^{Q36H} cDNA-T2A-*Luciferase* sequence (fig. S2A). Murine *Btg1* and human *BTG1* cDNA sequences are slightly different, but their protein sequence is 100% identical. The targeting vector was constructed as follows: The murine *Btg1*^{Q36H} cDNA-T2A-*Luciferase* sequence was first cloned into the MluI site of a pSa-stop-bGH polyA vector to generate the construct pSa-stop-*Btg1*^{Q36H} cDNA-T2A-*Luciferase*-bGH polyA. The stop cassette was LoxP-PGK/gb2 promoter-neo/kana resistance gene-PGK polyA-2X SV40 polyA signal-LoxP. The final cassette therefore consisted of a splice acceptor, a LoxP-flanked stop cassette, Btg1^{Q36H} cDNA-T2A-*Luciferase*, and a bGH polyA signal. Then, the entire cassette was inserted into the XbaI site (XbaI was disrupted by this insertion) of the pROSA26–1 vector using the Recombineering technology. The resulting targeting vector contained a short homology arm with a 1.08-kb *Rosa26* genomic sequence upstream of the cassette and a 4.34-kb-long homology arm downstream of the cassette. The targeting vector was confirmed by restriction analysis and sequencing after each modification. iTL IC1 (C57BL/6) embryonic stem cells were electroporated with this targeting vector, stable G418-resistant clones were derived and microinjected into BALB/c blastocysts. Resulting chimeras with a high-percentage black coat color were mated to wild-type C57BL/6N mice to generate F1 heterozygous offspring. Tail DNA was analyzed from pups with black coat color. Short homology arm integration, long arm junction, and targeted allele sequence were confirmed by PCR followed by gel electrophoresis and Sanger sequencing (Genewiz).

Conditional Btg1^{WTKI} mice (*R26*$^{lsl.Btg1wt}$) were generated at the MSKCC Mouse Genetics Core Facility by introducing a single-nucleotide substitution to revert the Q36H mutation of the cDNA sequence in *R26*$^{lsl.Btg1Q36H}$ mice to a wild-type allele, by CRISPR-Cas9–mediated genome targeting (fig. S2, D and E). Oocytes from 3- to 5-week-old R26$^{lsl.Btg1Q36H/lsl.Btg1Q36H}$ or *R26*$^{lsl.Btg1Q36H/+}$ superovulated females and spermfrom ≥2-month-old *R26*$^{lsl.Btg1Q36H/lsl.Btg1Q36H}$ males were used for in vitro fertilization. Resulting zygotes were injected with a mix of Cas9 protein (Integrated DNA Technologies), CRISPR RNA (crRNA, 5′-GGCTCTGGCTGAAAGTCTGC-3′), trans-activating CRISPR RNA (tracrRNA, 5′-AAACAGCAUAGCAAGUUAAAAUAAGGCUAGUCCGUUAUCAACUUGAAAAAGUGGCACCGAGUCGGUGCU-3′), and a 105–base pair (bp) donor oligo for homologous recombination (HR oligo, 5′-ATCTCCAAGTTCCTCCGCACCAAGGGGCTCACGAGCGAGCGACA**G**CTGCAGACTTTCAGCCAGAGCCTGCAGGAGCTGCTGGCAGAACATTACAAACATCACTGG-3′), which contained a C>G substitution (in bold in the above sequence) to revert H36 (CAC) to Q36 (CAG). The mutated C in Btg1^{Q36H} was also the third base of the protospacer adjacent motif (PAM) sequence on the reverse strand and therefore did not exist in the endogenous *Btg1* sequence or in the *Rosa26* wild-type reverted *R26*$^{lsl.Btg1wt}$ allele, preventing Cas9 recutting of the reverted allele. The C>G substitution also created a new PvuII site, which we used to genotype the pups. After injection, two-cell embryos were implanted into day 0.5 pseudo-pregnant females. Pups were then checked by PCR on genomic DNA and PvuII

digestion (fig. S2, E and F). Potential founders were further checked by Sanger sequencing (Genewiz).

The following strains were obtained from The Jackson Laboratory (Ben Harbor): C57BL/6J (CD45.2, stock 000664), B6.SJL-*Ptprc*^{a} *Pepc*^{b}/BoyJ (CD45.1, *SJL*$^{+/+}$, stock 002014), *Cd19*^{Cre} (32) (stock 006785), *Cg1*^{Cre} (38) (stock 010611), *Myc*^{GFP} (37) (stock 021935), B1–8^{hi} (33) (stock 007594), *DEC205*$^{-/-}$ (67) (stock 005528), *PA-GFP* (44) (stock 022486), and *mRFP1* (68) (stock 005884). The VavP-*Bcl2* (48) model was developed by J. M. Adams (Walter and Eliza Hall Institute of Medical Research, Australia).

Genotyping

PCR-based genotyping of the *R26*$^{lsl.Btg1Q36H}$ and *R26*$^{lsl.Btg1wt}$ alleles was performed on mouse tail lysates. Tail tips were lysed in DirectPCR lysis reagent (Viagen 102T) plus proteinase K during overnight incubation at 55°C with shaking, followed by 45 min incubation at 85°C (no shaking) to inactivate proteinase K. After a short spin, supernatant was used for PCR using Taq polymerase (Roche). The forward primer annealed to the *Rosa26* short homology arm upstream of the cassette and was combined with two reverse primers. The first one annealed to the 5′ LoxP site of the targeted allele, and the second one annealed to the *Rosa26* long homology arm downstream of the cassette and amplified only the nontargeted allele (because of a >5 kb distance with the forward primer in the targeted allele). Details about primers are included in table S8. The PCR program was 94°C for 2 min, [94°C for 30 s, 65°C for 30 s, and 72°C for 1 min] for 40 cycles, and 72°C for 7 min. Genotyping for *R26*$^{lsl.Btg1Q36H}$ and *R26*$^{lsl.Btg1wt}$ alleles, as well as all other mouse alleles used in this study, was also done by Transnetyx using reverse transcription quantitative polymerase chain reaction (RT-qPCR).

RNA extraction

Cells were collected from culture and resuspended in TRIzol (Invitrogen 15596018), or cells were sorted directly into TRIzol LS (one third more concentrated TRIzol reagent, Invitrogen 10296028), and total RNA was extracted. Purified RNA was resuspended in molecular-grade RNase-free water and analyzed on Nanodrop and Qubit Fluorometric Quantification for quality check and concentration measurement, respectively.

qPCR

cDNA synthesis was performed with equal amounts of total RNA for all samples in each experiment, using the Verso cDNA Synthesis kit (Thermo Fisher AB1453B). RT-qPCR was performed using same volume of cDNA for all samples, on a QuantStudio6 Flex Real-Time PCR System (Thermo Fisher) with Fast SYBR Green Master Mix (Thermo Fisher 4385614). Each biological replicate (either independently generated DLBCL lines or individual mouse samples) was further analyzed in triplicate wells to assess technical variability, of which only the mean was used to calculate the mean ±SD between biological replicates. mRNA expression levels of genes of interests were normalized to that of *TBP* and/or *GAPDH*, as specified, using the delta-delta Ct method. Details about primers used are included in table S8.

Presence of Cre-recombined alleles

Cre-mediated recombination of *R26*$^{lsl.Btg1Q36H}$ and *R26*$^{lsl.Btg1wt}$ alleles was validated on gDNA extracted from sorted naïve B cells and germinal center B cells or from B220^{+}-enriched B cells as indicated, using Puregene Gentra cell kit (QIAGEN 158388). B220^{+} B cells were enriched by positive selection with anti-B220 magnetic beads (Miltenyi Biotec 130-049-501). We performed PCR on gDNA using primers that specifically amplified the recombined targeted allele and Phusion HF polymerase (NEB M0530). The PCR program was 98°C for 30 s, [98°C for 15 s, 70°C for 30 s, and 72°C for 30 s] for 30 cycles, and 72°C for 10 min. PCR products were resolved by agarose gel electrophoresis and visualized on a ChemiDoc Touch imaging system (BioRad) using SYBR Safe DNA stain (Thermo Fisher S33102). The same primers were used to confirm expression of Cre-recombined alleles on total RNA extracted from B220^{+}-enriched B cells, reverse transcribed, and analyzed by qRT-PCR. Forward primer annealed to the Rosa26 short homology arm upstream of the cassette and reverse primer to the kozak sequence and Btg1 coding sequence from the *R26*$^{lsl.Btg1Q36H}$ or *R26*$^{lsl.Btg1wt}$ at the *Rosa26* locus (fig. S2, A and D), to ensure only recombined targeted alleles and transcripts were amplified from gDNA and total RNA, respectively. Primer details are included in table S8.

Efficiency of Cre-recombination

The proportion of recombined *R26*$^{lsl.Btg1Q36H}$ allele was measured in the competitive setup using adoptive transfer of B cells with an endogenous BCR repertoire into WT recipient mice. We sorted Q36H naïve B cells (NB) as live B220^{+}IgD^{+}CD45.2 and germinal center B cells (GC B) as live B220^{+}FAS^{+}CD38^{-}CD45.2 from the spleens of CD45.1 recipient mice at day 21 after immunization, when Q36H GC B cells are outcompeting WT recipient cells. gDNA was extracted using Puregene Gentra cell kit (QIAGEN 158388) with volumes adapted for low material. For each sample, a minimum of 240 pg gDNA per well, as measured by Qubit dsDNA HS (Invitrogen Q32854), was used for qPCR amplification using two sets of primers, the first one specifically amplifying the recombined alleles (same as above for PCR on gDNA or for qPCR on cDNA) and the second one specifically amplifying the non-recombined alleles, sharing the forward primer with the first set, but with the reverse primer annealing to the STOP cassette (fig. S7D). Primer details are included in table S8. A standard curve for each of these primer sets was generated, using their corresponding double-stranded DNA (dsDNA) amplicons to the amount of 10^3 to 10^8 absolute copy number per well. The efficiency of Cre-mediated recombination was calculated as the absolute copy number of recombined alleles over the absolute copy number of recombined plus non-recombined alleles.

IgH rearrangement

For clonal variance analysis in the lymphomagenesis study cohort, GC B cells from Bcl2-only and Bcl2+Q36H mice were sorted as live B220^{+}FAS^{+}GL7^{+} cells from PNA^{+} enriched splenocytes on BD Influx or BD FACSAria II, 8 months after transplantation. We extracted RNA and synthesized cDNA using equal amounts of RNA for all samples, as described above. In parallel, we processed centroblasts sorted from a wild-type mouse that had been immunized 9 days before with 2% SRBC, to use as a nontumor control. We

then performed PCR on equal volume of cDNA for all samples with GoTaq Flexi DNA Polymerase (Promega M8295) to amplify the VHQ52-JH4 and VH7183-JH4 regions of the *IgH* locus, using a set of forward primers that annealed to the framework region of one of the most abundantly used IgVH gene families and a reverse primer annealing to the JH1–4 gene segments, as described before (69). Each sample was amplified in duplicates, both of which were resolved by agarose gel electrophoresis on adjacent lanes and visualized on a ChemiDoc Touch imaging system using SYBR Safe DNA stain. The PCR program was 95°C for 2 min, [95°C for 45 s, 60°C for 45 s, and 72°C for 2 min] for 40 cycles, and 72°C for 10 min. Primer details are included in table S8.

Immunizations

To induce GC formation in draining lymph nodes, mice were immunized by subcutaneous injection of the highly substituted hapten NP conjugated to the carrier protein ovalbumin (OVA), NP(16–19)-OVA (Biosearch Technologies N-5051), either into the hind footpad for popliteal lymph nodes collection, or into the base of tail for inguinal lymph nodes collection. We did not observe differences in GC response after NP-OVA immunization in popliteal versus inguinal lymph nodes. In noncompetitive setup, non-B1–8^{hi} mice were injected with 50 μg of NP(16–19)-OVA. In competitive setup, recipients of B1–8^{hi} adoptively transferred B cells were injected 24 hours after transfer with 20 μg of NP(16–19)-OVA subcutaneously for T-dependent stimulation, or with 50 ug of NP(44)-Ficoll (Biosearch Technologies F-1420) intraperitoneally for T cell–independent stimulation. Conjugated NP-OVA or NP-Ficoll was absorbed in alum adjuvant (Thermo Fisher 77161) at a 1:3 ratio of alum:immunogen prior to injection.

To induce germinal center (GC) formation in spleens, mice were immunized by intraperitoneal injection of 500 ml of 2% SRBCs resuspended in sterile 1X Dulbecco's phosphate-buffered saline (DPBS) from a solution of sheep blood in Alsever's (Cocalico Biologicals 20–1334A), or by intraperitoneal injection of 80 μg NP(30–32) conjugated to the carrier protein keyhole limpet hemocyanin (KLH) (Biosearch Technologies N-5060) absorbed in alum adjuvant (Thermo Fisher 77161) at a 1:1 ratio of alum:immunogen prior to injection.

For the experiments with in vivo targeted delivery of T cell help, recipients of a mixture of B1–8^{hi}; *DEC205*$^{+/+}$ and B1–8^{hi}; *DEC205*$^{-/-}$ adoptively transferred B cells were primed by intraperitoneal injection of 50 μg OVA (Biosearch Technologies O-1000) absorbed in alum at a 1:2 ratio of alum:immunogen 2 to 4 weeks prior to the transfer and received a boost immunization by subcutaneous injection of 50 μg NP(19)-OVA without alum into the hind footpad 24 hours after transfer. At the indicated times at days 6 and 7 after boost, mice received 5 μg of anti-DEC-OVA chimeric antibody diluted in phosphate-buffered saline (PBS) by subcutaneous injection into the hind footpad, and popliteal lymph nodes were analyzed at day 9 after boost. Anti-DEC-OVA was produced by transient transfection of HEK293T cells as previously described (70).

Competitive adoptive cell transfers

Spleens from mice of the indicated genotypes were mashed and filtered through a 40 μm cell strainer. After treatment with red blood cell lysis solution (QIAGEN 158904), splenocytes were filtered into PBS supplemented with 0.5% bovine serum albumin (BSA) and 2 mM EDTA (PBE). Resting B cells were isolated by negative selection with magnetic cell separation using anti-CD43 beads (Miltenyi Biotec 130-049-801). To determine the proportion of NP-binding B1–8^{hi} cells, we stained a fraction of cells with 5 μg/ml NP(16)-PE (Biosearch Technologies N-5070) and analyzed them by flow cytometry. We then adoptively transferred a total number of isolated B cells corresponding to 0.3×10^6 to 0.5×10^6 NP-binding B cells per recipient, by intravenous injection through the retro-orbital venous sinus, at the proportions indicated in the experimental schematic for each relevant figure. Alternatively, for the transfer of non-B1–8^{hi} mature B cells, we directly adoptively transferred a total number of 20 million isolated B cells per recipient by intravenous injection through the retro-orbital venous sinus.

To measure the proliferation rate of adoptively transferred B cells responding to NP-Ficoll immunization, isolated resting B1–8^{hi} B cells from both genotypes were mixed at equal proportions of NP-binding cells, stained with CellTrace CFSE (Invitrogen C34554) at a final concentration of 5 μM in PBS for 10 min at 37°C, and washed with PBE prior to injection into recipients.

Bone marrow and fetal liver cell transplantation

For lymphomagenesis studies, we transplanted bone marrow cells (Bcl2$^{+/-}$Q36H cohort) or fetal liver cells (Bcl2$^{+/-}$WTKI cohort) from donors of the indicated genotypes into lethally irradiated C57BL/6J females (two doses of 450 rad, on a RS 2000 Biological Research X-ray Irradiator, Rad Source Technologies). Bone marrow cells were harvested from the tibias and femurs of donor mice, filtered through a 40 μm mesh, treated with red blood cell lysis solution (QIAGEN 158904), counted, and frozen down as viable cells at a density of <15 million cells/ml. Genotype of donor mice was double checked by PCR and gel electrophoresis before thawing and transplantation. Fetal livers were isolated from E14.5 embryos and dissociated between the frosted, sandblasted ends of two sterile glass slides (VWR 48312–024). Fetal liver cells were filtered through a 35 μm mesh, counted, and frozen down as viable cells. Genotyping was performed on embryo head lysates prepared the same way as tail tip lysates, by PCR and gel electrophoresis.

Bone marrow or fetal liver cells were then thawed and cultured at 5 million/ml for 2 hours at 37°C in RPMI with 10% fetal bovine serum (FBS), 50 U/ml penicillin, 50 μg/ml streptomycin, freshly added beta-mercaptoethanol at 55 μM, interleukin-3 (IL-3) at 6 ng/ml (R&D Systems 403-ML), SCF at 10 ng/ml (R&D Systems 455-MC), IL-6 at 10 ng/ml (PeproTech 216–16) and IL-7 at 5.4 ng/ml (R&D Systems 407-ML). Cells were then collected, washed three times with 1X DPBS, counted, and resuspended in 1X DPBS for intravenous injection of 1 million bone marrow cells or 0.24 million fetal liver cells in 100 μl per lethally irradiated recipient, through the retro-orbital venous sinus. After 2 months, fully engrafted mice were immunized monthly by intraperitoneal injection of 500 ml of 2% SRBC in sterile 1X DPBS for 3 or 8 months, as specified, to induce GC

formation. With the exception of mice euthanized at 8 months where indicated, all mice involved in lymphomagenesis studies were monitored until any one of several criteria for euthanizing were met, including severe lethargy, more than 10% body weight loss, or palpable splenomegaly that extended across the midline.

Live and in situ mouse imaging

Luciferase reporter imaging in live animals carrying the *R26*$^{\text{dsl.Btg1Q36H}}$ or *R26*$^{\text{dsl.Btg1wt}}$ allele and in situ imaging was performed on an IVIS SpectrumCT In Vivo Imaging System instrument (PerkinElmer) using the Living Image software (PerkinElmer). Mice were injected intraperitoneally with 2.5 mg of luciferin substrate (200 μl at 12.5 mg/ml, Promega P1043) and anesthetized with 2% isoflurane. Bioluminescence signal (radiance, in photons per second per square centimeter per steradian) was acquired 15 min after injection of luciferin. For each experiment, images were set to the same scale and total luminescence signal (flux, in photons per second) was quantified using one region of interest per mouse in the Living Image software. For in situ imaging, mice were euthanized, immediately injected intraperitoneally with 2.5 mg of luciferin substrate, opened in the intraperitoneal area to expose the spleens and surrounding lymph nodes, and imaged within 2 min of euthanasia.

H&E staining and immunohistochemistry

Mouse organs were fixed in 10% neutral buffered formalin (Sigma) for 24 to 48 hours and transferred to 70% ethanol. Tissues were then embedded in paraffin, processed, and stained at the Laboratory of Comparative Pathology [Weill Cornell Medicine (WCM)/Memorial Sloan Kettering Cancer Center (MSKCC)]. Briefly, 5 μm sections were deparaffinized and stained with hematoxylin and eosin (H&E) or processed for immunohistochemistry by heat antigen-retrieval in citrate buffer at pH 6.4, followed by treatment with 3% hydrogen peroxide in methanol to block endogenous peroxidase (HRP) activity. Indirect immunohistochemistry was then performed using biotinylated peanut agglutinin (PNA, Vector Laboratories B1075) or anti-species-specific biotinylated secondary antibodies, followed by avidin-horseradish peroxidase and development with DAB substrate (Vector Laboratories). Sections were counterstained with hematoxylin. The following primary antibodies were used: anti-B220 (BD 550286) and anti-Ki67 (Cell Signaling Technology 12202). Slides were scanned using a Zeiss Mirax Slide Scanner, and photo-micrographs were examined using Aperio eSlide Manager (Leica Biosystems). QuPath software (71) was used to quantify GC areas.

Flow cytometry analysis and cell sorting

Spleens were mashed and bone marrow cells were flushed from tibias and femurs. Splenocytes and bone marrow cells were filtered through a 40 μm cell strainer and treated with red blood cell lysis solution (QIAGEN 158904). Resulting single-cell suspensions were resuspended in PBE with 0.5 μg/ml rat anti-mouse CD16/CD32 (clone 2.4G2, BD) and incubated for ≥5 min on ice to block Fc receptors. Lymph node cells were directly mashed into the Fc block mix using pellet pestles (Sigma Z359947). Peritoneal B cells were collected by injecting 9 ml of PBS with 0.5% BSA into the peritoneal cavity followed by a subcostal incision and aspiration of the peritoneal cell suspension. After centrifugation, cells were stained for 20 min on ice, in a mix of fluorochrome-conjugated anti-mouse

antibodies diluted either in PBE, or in a 50:50 mixture of Brilliant Stain Buffer (BD 566349) and PBS with 0.5% BSA but without EDTA when the mix contained ≥2 BV- or BUV-conjugated antibodies, to avoid staining artifacts resulting from interaction between these fluorescent dyes. For phosphorylated S6 (pS6) staining, incubation was precisely timed to prevent time-related variations in dephosphorylation by endogenous phosphatases, as previously described (5). Cells were first stained for surface markers and then fixed and permeabilized. Fixation and permeabilization using Cytofix/Cytoperm (BD 554722) was timed to occur exactly 30 min after euthanasia for each mouse. We then stained with anti-pS6 diluted in Perm/Wash (BD 554723) for 2 hours. All cells were then washed twice before analysis. DAPI (4′,6-diamidino-2-phenylindole; Thermo Fisher D1306) was added just before acquisition at final 0.5 μg/ml for the exclusion of dead cells. Data were acquired on BD FACS Canto II, BD Fortessa, BD Symphony A5 or BD Symphony A3 and analyzed using FlowJo software package (TreeStar).

For MYC flow cytometry analyses in cell lines, two or three independently generated and validated SU-DHL4 stable lines for each indicated genotype were set at 1 million cells per ml in fresh complete RPMI and incubated at 37°C for 46 hours, for cells to have just doubled. For MYC flow cytometry analyses in human primary GC B cells freshly immortalized, cells were plated at 1 million cells per ml onto fresh feeders and incubated at 37°C for 3 or 4 days. MG132 (Selleck S2619) was then added to cells at 5 μM final MG132. Samples were collected at the indicated times after treatment and immediately fixed for 1 hour at room temperature or overnight at 4°C for all samples, depending on experiments (this did not affect results) using the True-Nuclear Transcription Factor Buffer Set (Biolegend 424401). Cells were then washed twice in 1X perm buffer and kept at 4°C. Fixed and permeabilized cells were blocked with 2% normal goat serum (Cell Signaling Technology 5425) diluted in perm buffer, for 15 min at room temperature. We then stained cells with AF647 anti-MYC (rabbit, clone Y69, Abcam ab190560, diluted to 0.71 μg/ml) for 30 min at room temperature in the dark. Alternatively, we stained cells with unconjugated anti-MYC (rabbit, clone Y69, Abcam ab32072, diluted to 0.45 μg/ml), washed twice with perm buffer, and incubated with AF647 anti-rabbit secondary antibody (Life Technologies A21246, diluted to 2 μg/ml) for another 30 min at room temperature in the dark. We used the following isotype control IgGs at the same concentration as their corresponding anti-MYC antibodies: Abcam ab199093, clone EPR25A, for the AF647 anti-MYC antibody; and Abcam ab172730, clone EPR25A, for the unconjugated anti-MYC antibody. After two washes in perm buffer, we resuspended cells in perm buffer and analyzed them.

For cell sorting from spleen and lymph nodes, cell suspensions were prepared and stained as for flow cytometry analysis, except that splenocytes were pre-enriched either for $B220^+$ B cells by positive selection with anti-B220 magnetic beads (Miltenyi Biotec 130-049-501) or for GC B cells by positive selection with PNA magnetic beads (Miltenyi Biotec 130-110-479) where specified. The indicated populations were then isolated on a BD FACSAria II or a BD Influx sorter at the Flow Cytometry core (WCM) or in the laboratory.

The following antibodies were used: APC-Cy7 anti-B220 (clone RA3–6B2, BioLegend 103224, dilution 1:500), BV786 anti-B220 (clone RA3–6B2, BD 563894, dilution 1:300), FITC anti-human CD2 (clone RPA-2.10, BD 556608, dilution 1:100), BV605 anti-CD5

(clone 53–7.3, BD 563194, dilution 1:500), APC-Cy7 anti-CD19 (clone 6D5, BioLegend 115530, dilution 1:200), FITC anti-CD19 (clone 1D3, BD 553785, dilution 1:500), PE-Cy7 anti-CD21 (clone 7E9, BioLegend 123420, dilution 1:500), FITC anti-CD23 (clone B3B4, BD 553138, dilution 1:500), PE-Cy7 anti-CD25 (clone PC61, BD 561780, dilution 1:500), APC anti-CD38 (clone 90, eBioscience 17-0381-81, dilution 1:500), BUV395 anti-CD38 (clone 90, BD 740245, dilution 1:500), BUV395 anti-CD45.1 (clone A20, BD 565212, dilution 1:200), PerCP-Cy5.5 anti-CD45.1 (clone A20, eBioscience 45-0453-82, dilution 1:200), AF647 anti-CD45.2 (clone 104, BioLegend 109818, dilution 1:500), APC anti-CD45.2 (clone 104, BioLegend 109814, dilution 1:400), PE-Cy7 anti-CD45.2 (clone 104, eBioscience 25-0454-82, dilution 1:300), biotin anti-CD83 (clone Michel-19, BioLegend 121504, dilution 1:200), BV605 anti-CD86 (clone GL-1, BioLegend 105037, dilution 1:200), PE-Cy7 anti-CD86 (clone GL-1, BioLegend 105014 or BD 560582, dilution 1:200), BUV737 anti-CD138 (clone 281–2, BD 564430, dilution 1:500), APC anti-c-Kit/CD117 (clone 2B8, BD 561074, dilution 1:500), biotin anti-CXCR4 (clone 2B11, BD 551968, dilution 1:200), PE anti-CXCR4 (clone 2B11, BD 561734, dilution 1:100), BV421 anti-FAS (clone Jo2, BD 562633, dilution 1:300), PE-Cy7 anti-FAS (clone Jo2, BD 557653, dilution 1:500), AF647 anti-GL7 (clone GL7, BD 561529, dilution 1:500), AF647 anti-MYC (rabbit, clone Y69, Abcam ab190560, diluted to 0.71 μg/ml), unconjugated anti-MYC (rabbit, clone Y69, Abcam ab32072, diluted to 0.45 ug/ml) and AF647 anti-rabbit secondary antibody (Life Technologies A21246, diluted to 2 μg/ml), BV510 anti-IgD (clone 11–26c.2a, BD 563110, dilution 1:500), PE anti-IgD (clone 11–26c.2a, BD 558597, dilution 1:500), PerCP-Cy5.5 anti-IgD (clone 11–26c.2a, BioLegend 405710, dilution 1:500), APC anti-IgG1 (clone A85–1, BD 560089, dilution 1:500), BV421 anti-IgG1 (clone A85–1, BD 562580, dilution 1:500), BV650 anti-IgG1 (clone RMG1–1, BioLegend 406629, dilution 1:500), APC anti-IgM (clone II/41, eBioscience 17-5790-82, dilution 1:500), BV711 anti-IgM (clone II/41, BD 743327, dilution 1:500), BV421 anti-Ig lambda light chain (l1, l2, l3, clone R26–46, BD 744523, dilution 1:400), AF647 anti-pS6 (S6 phosphorylated at S235/236, clone D57.2.2E, Cell Signaling Technology 4851, dilution 1:200), APC streptavidin (BioLegend 405207, dilution 1:300) and PE-Cy7 streptavidin (eBio-science 25-4317-82, dilution 1:400).

To assess progression through S phase of the cell cycle, we performed dual nucleotide pulse and staining as previously described (46). Briefly, mice were injected intravenously with 1 mg of EdU (Thermo Fisher E10187) and 1 hour later with 2 mg BrdU (Sigma B5002). Thirty minutes after the second injection, lymph nodes were harvested, and single cell suspensions were prepared. After cell surface staining as described above, cells were fixed and permeabilized using BD Cytofix/Cytoperm and BD Permeabilization Buffer Plus. EdU and BrdU incorporation into DNA was assayed using the Click-iT EdU Pacblue Flow Cytometry Assay Kit (Thermo Fisher C10418) and AF647 mouse anti-BrdU (clone 3D4, BD 560209), respectively.

EdU staining on a slide

Mice were injected intravenously through the retro-orbital venous sinus with 1 mg EdU (200 μl at 5 mg/ml) 1 hour before euthanasia. Spleens were processed and splenocytes stained and sorted as described above. Myc^{GFP+} and Myc^{GFP-} GC B cells were sorted on a BD FACSAria II into PBE and immediately spun onto positively charged glass

slides (VWR 48311–703) by cytospin using an Aerospray Pro slide stainer/cytocentrifuge (ELITechGroup) and left to air dry for 2 hours. Cells were fixed with 4% paraformaldehyde for 15 min at room temperature, washed three times with PBS, and left to dry overnight at room temperature. Cells were then washed using PBS plus 3% BSA and permeabilized using 0.5% triton-X for 20 min. EdU was detected using Click-iT Plus EdU Cell Proliferation Kit for Imaging, AF647 dye (Thermo Fisher C10640). This included a staining step with DAPI at 1 μg/ml final. Aqueous mounting media (Fluoromount, Sigma F4680) and coverslips (VWR micro cover glass) were applied to slides right after staining, and imaging was performed immediately.

Images were acquired on a Zeiss LSM 880 laser scanning confocal microscope with a 10× objective lens using 405 nm and 633 nm laser excitation for DAPI and AF647, respectively, using the Zen software (Zeiss). Alternatively, images were acquired on an Evos FL Digital inverted fluorescence microscope (Life Technologies) with a 10× objective lens, a high-sensitivity monochrome camera (Sony ICX285AL CCD) and DAPI and Cy5 Evos light cubes to detect DAPI and AF647, respectively. Representative images shown were acquired on the Evos instrument. All images were viewed and processed using the Fiji software (72). Cyan and magenta lookup tables (LUTs) were applied to DAPI and AF647 channels, respectively, for visualization.

Generation of stable DLBCL cells

All constructs (EF1a-hBTG1, EF1a-hBTG1^{Q36H}, EF1a-EV, EF1a-hBTG1-V5, EF1a-hBTG1^{Q36H}-V5, and EF1a-EGFP-V5) were cloned into the pLEX_307 vector (a gift from D. Root, Addgene 41392), which drives constitutive lentiviral expression of the open reading frames (ORFs) as fusion proteins with a C-terminal V5 epitope tag under the control of the EF1-alpha promoter, as well as puromycin resistance. ORFs with a stop codon were used to express nontagged proteins, and ORFs lacking a stop codon were used to express V5-tagged proteins. Human BTG1 ORF with stop codon was obtained in pENTR221 vector (Transomic) and used to PCR amplify BTG1 ORF without stop codon. Q36H mutation was introduced into BTG1 with or without stop codon by site-directed mutagenesis using Phusion HF polymerase (NEB) followed by DpnI digestion. An empty control vector (EV) was generated by NotI/AscI double digestion of an ORF-containing pENTR/D-TOPO vector, followed by blunting with T4 DNA polymerase and ligation. EGFP ORF without stop codon was obtained in pENTR221 [a gift from D. Root, Addgene 25899 (73)]. All of the above entry vectors were recombined into the pLEX_307 destination vector using the Gateway LR Clonase II enzyme mix (Invitrogen 11791–020). T39I, S43N, and A49T mutations were introduced into BTG1-V5 by site-directed mutagenesis using Phusion HF polymerase (NEB) followed by DpnI digestion. Identity of all vectors was verified by Sanger sequencing (Genewiz).

For lentivirus production, 2.5 million HEK293T cells cultured in complete Dulbecco's modified Eagle medium [DMEM (Thermo Fisher 11965118); 10% FBS, 2 mM glutamine, 50 U/ml penicillin, and 50 μg/ml streptomycin] were plated in a 10-cm-diameter plate for 24 hours before cotransfection with the expression construct, pMD2.G, and psPAX2 vectors at a 4:1:3 ratio using Fugene HD (Promega E2311) for a total of 8 μg DNA per plate. After

12 to 16 hours, medium was replaced. Virus-containing medium was collected at 48 and 72 hours after transfection, pooled, filtered, concentrated using PEG-it (System Biosciences LV825A-1), and resuspended at 20X in 1X DPBS. Virus was used right away or stored aliquoted at −80°C.

SU-DHL4 cells cultured in complete RPMI (10% FBS, 2 mM glutamine, 50 U/ml penicillin, 50 μg/ml streptomycin, and 10 mM HEPES) were transduced at a multiplicity of infection of 1 by adding concentrated virus to freshly plated cells. After 72 hours incubation, medium was replaced with fresh medium containing 1 μg/ml puromycin, and cells were selected for 7 days, with fresh addition of puromycin-containing medium every other day. Expression of the constructs was validated by qRT-PCR and Western blot (WB) from an equal number of cells from cell suspension cultures.

Generation of stable human primary GC B cells

Fresh human tonsils were collected from the Department of Pathology at Weill Cornell/New York Presbyterian (IRB protocol 0804009763). To generate human primary GC B cells stably expressing $BTG1^{WT}$ versus $BTG1^{Q36H}$, we adapted a procedure previously described in detail (43). This involved isolating GC B cells from human tonsils, immortalizing them through BCL2/BCL6 retroviral transduction (the $CD2^{+}$ marker was used to identify immortalized cells), and stably expressing V5-tagged $BTG1^{WT}$, $BTG1^{Q36H}$, or EGFP through lentiviral transduction and puromycin selection (fig. S11D).

Tonsillar GC B cells were purified using human B cell negative selection isolation Kit II (Miltenyi Biotec 130-051-151) with addition of IgD-BIOT (SouthernBiotech 9030–08, dilution 1:100) and CD44-BIOT (SouthernBiotech 9400–08, dilution 1:100) antibodies to remove naïve and memory B cells. Purified GC B cells were cultured in RPMI (20%, 2 mM glutamine, 50 U/ml penicillin, 50 μg/ml streptomycin) at a concentration of 1 million cells per ml, on irradiated (30 Gy) YK6-CD40Lg-IL21 feeder cells that carry puromycin resistance (0.2 million cells per ml). GC B cells were replated every 3 to 4 days on freshly irradiated YK6 feeder cells.

For virus production, Lenti-X 293T cells were plated in a 10-cm^2 dish 16 hours before transfection at 0.2 million cells per ml in DMEM (10%, 2 mM glutamine, 50 U/ml penicillin, 50 μg/ml streptomycin). For retrovirus production (BCL2-BCL6), vectors were mixed as followed: 1 μg of pHIT60 (gag-pol), 1 μg of phCMV-GaLV MTR [a gift from D. Hodson, Addgene 163612 (74)] and 4 μg of MSCV-BCL6-t2A-Bcl2 [a gift from D. Hodson, Addgene 135305 (74)] and incubated for 45 min in 1 ml Opti-MEM with 18 μl of Trans-IT (Mirus Bio MIR 2300) before addition to the Lenti-X 293T dish. For lentivirus production (V5-tagged $BTG1^{WT}$, $BTG1^{Q36H}$, EGFP), 8.3 μg of gag-pol vector pCMVDeltaR8.91, 2.8 μg of envelop vector phCMV-GaLV MTR [a gift from D. Hodson, Addgene 163612 (74)], and 11 μg of BTG1 constructs in pLEX_307 vector (described above for cell lines) were incubated for 45 min in 1 ml Opti-MEM with 33 μl of Trans-IT (Mirus Bio, MIR 2300) and added to the Lenti-X 293T dish. Viruses were collected and filtered (0.45 μm) 72 hours later and frozen or directly used for infection of GC primary cells.

For infection, 2 million GC B target cells with feeder cells were directly resuspended in virus suspension at a virus:media ratio of 1:4 for retrovirus or 3:4 for lentivirus, with addition of 8 μg/ml of polybrene (Santa Cruz sc-134220) and 25 μM HEPES. Cells and virus mixtures were plated in 12-well plates and centrifuged at 1500*g* for 90 min at 32°C. Virus-containing medium was replaced with fresh medium (RPMI 20%, 2 mM glutamine, 50 U/ml penicillin, 50 μg/ml streptomycin) immediately after centrifugation for retroviral infection and at least 4 hours after centrifugation for lentiviral infection (43). Seventy-two hours after lentiviral infections, cells were treated with 1 μg/ml puromycin for 10 days to select for transduced cells. BCL2-BCL6 positivity was continuously monitored by anti-CD2 flow cytometry. Experiments were performed when >95% puromycin-selected cells were obtained within $CD2^+$ GC B cells.

mRNA stability assay

Three independently generated and validated SU-DHL4 stable lines for each indicated genotype were set at 1 million cells per ml in fresh complete RPMI and incubated at 37°C for 24 hours, for cells to be growing exponentially and at similar medium composition at the time of treatment. Cells were then collected (0 hours) or actinomycin D (Cell Signaling Technology 15021) was added at 10 μg/ml final and cells were collected at the indicated time points after treatment. Upon collection, cells were spun and directly resuspended in TRIzol for RNA extraction, followed by cDNA synthesis and qRT-PCR analysis as described above.

RNA immunoprecipitation (RIP)

Two or three independently generated and validated SU-DHL4 stable lines were used for each indicated genotype per experiment. Thirty-five million cells per sample were set at 1 million cells per ml in fresh complete RPMI and incubated at 37°C for 24 hours, for cells to be growing exponentially and at similar medium composition at the time of treatment. Cells were collected, washed twice with cold 1X DPBS, and lysed in 175 μl Magna RIP lysis buffer (from Millipore 17–700) with frequent vortexing for 10 to 30 min on ice. Lysates were directly processed for RIP using magnetic beads, following the Magna RIP kit instructions (Millipore 17–700) or kept at −80°C until processing. Anti-V5 mouse antibody (7.5 μg; Abcam 27671) was used to pull down $BTG1^{WT}$-V5, $BTG1^{Q36H}$-V5, or EGFP-V5 (negative control). Ten percent of lysate was saved pre-RIP as input RNA, 175 μl lysate was RIPed, and the remaining lysate volume was saved for protein quantification by Bradford to analyze by Western blot as input protein. Post-RIP, 6% of the beads suspension was saved during the last wash to analyze by Western blot as RIP protein. RNAs were purified from the beads and input RNA samples according to the Magna RIP kit instructions and resuspended in 25 μl molecular grade RNase-free water. Equal RNA amounts were then used for cDNA synthesis and qRT-PCR as described above. In the first experiment, RIP was done in technical duplicates for each independent line (35 million cells each, two independent lines per genotype). We observed highly similar pull-down efficiency between technical duplicates (compare a and b replicates, fig. S9A), and thus subsequent experiments were done with three independent lines and one RIP per genotype.

Western blot

Three independently generated and validated SU-DHL4 stable lines for each indicated genotype were set at 1 million cells per ml in fresh complete RPMI and incubated at 37°C for 24 hours, for cells to be growing exponentially and at similar medium composition at the time of treatment. For the starvation analyses, after the initial 24 hours incubation, cells were resuspended in fresh complete RPMI without FBS, incubated for 4 hours at 37°C, followed by resuspension in fresh complete RPMI (with 10% FBS) for 15 min, 30 min, 1 hour, and 2 hours, at which times cells were collected, spun, and directly lysed in lysis buffer (50 µl per million cells set up). For the newly protein synthesis analyses, after the initial 24 hours incubation, DMSO or MG132 (Selleck S2619) was added to cells for 5 µM final MG132 (and 0.01% DMSO final for all samples), and samples were collected at the indicated times after treatment, spun, and directly lysed in lysis buffer (50 µl per million cells plated). For the protein stability analyses, after the initial 24 hours incubation, CHX (stock kept in −80°C at 20 mg/ml in H_2O, Santa Cruz Biotechnology 66-81-9) was added to cells at 40 µg/ml final, and samples were collected at the indicated times after treatment, spun, and directly lysed in lysis buffer (50 µl per million cells plated). After development and signal quantification as described below, nonlinear regression curves were generated using exponential one phase decay equation with plateau constraint to zero.

Lysis buffer composition was 20 mM HEPES KOH pH 7.5, 50 mM b-glycerophosphate, 1 mM EDTA pH 8.0, 1 mM EGTA pH 8.0, 0.5 mM Na3VO4, 100 mM KCl, 10% glycerol, and 1% Triton X-100, supplemented with complete protease inhibitor cocktail (Roche). Protein concentration was determined by Bradford (Thermo Fisher 23236) and equal protein amounts were separated by 10 or 12% SDS–polyacrylamide gel electrophoresis. After electrophoretic transfer to BioTrace NT pure nitrocellulose blotting membrane (PALL 66485), membranes were stained with Ponceau, rinsed and blocked with 5% nonfat dry milk (Biorad 1706404) unless indicated otherwise, in PBS containing 0.1% Tween-20. Proteins were probed by overnight incubation at 4°C with the following antibodies: anti-V5 for Western blot after RIP (rabbit, Sigma V8137, dilution 1:2000), anti-V5 for all other Western blots (mouse, abcam 27671, dilution 1:2500), anti-alpha-tubulin (mouse, Sigma T6199, dilution 1:5000), anti-beta-actin (mouse, Sigma 5441, dilution 1:15,000), anti-MYC (rabbit, Cell Signaling Technology 5605, 1:1000), or anti-RPS3 (rabbit, Cell Signaling Technology 9538, 1:3000 in 5% BSA). Membranes were then incubated with HRP-conjugated anti-mouse or anti-rabbit secondary antibody (Cell Signaling Technology 7076 or 7074) or with IRDye 800CW anti-rabbit antibody (LI-COR 926–32211) for RPS3 detection. Development was done with ECL (Thermo Fisher 32106) for HRP-conjugated antibodies or directly for IRDye 800CW, either on a ChemiDoc Touch imaging system, ChemiDoc MP Imaging System (BioRad) or using Amersham Hyperfilm (Thermo Fisher 45001508) and a developer. Protein band intensities were quantified using the chemi-luminescence images acquired on the ChemiDoc and the Image Lab software v6.1.0 (Bio-Rad).

Cell volume measurement on Coulter counter

Three independently generated and validated SU-DHL4 stable lines for each indicated genotype were set at 1 million cells per ml (in triplicates or quadruplicates) in fresh complete RPMI and incubated at 37°C for 24 hours. Cells were then resuspended, and

an aliquot of cell suspension was used immediately for cell volume (mean fL) analysis on a Multisizer 4e Coulter particle analyzer (Beckman Coulter B43905).

Polysome profiling

Three independently generated and validated SU-DHL4 stable lines for each indicated genotype were set at 1 million cells per ml in fresh complete RPMI and incubated at 37°C for 48 hours. Equal numbers of cells for each line (30 million or 100 million cells, depending on experiment replicate) were treated with CHX at 100 μg/ml for 10 min at 37°C. Cells were then lysed on ice for 10 min in 400 μl lysis buffer containing 20 mM Tris HCl pH 7.4, 100 mM KCl, 5 mM $MgCl_2$, 1% TritonX-100, 100 μg/ml CHX, 10 mM DTT, EDTA-free protease inhibitors (Roche 11873580001,) and 500 U/ml RNasin RNase inhibitor (Promega N2611). Lysates were cleared by centrifugation at 15,000*g*, 4°C for 15 min. Cleared lysate aliquots were saved as inputs, and remaining cleared lysates were loaded onto a linear 20 to 50% sucrose gradient in 40 mM Tris HCl pH 7.5, 300 mM KCl, 20 mM $MgCl_2$, and 100 μg/ml CHX. Samples were then centrifuged at 42,000 rpm for 3 hours at 4°C using a TH641 rotor (Sorvall) in a Sorvall wX+ Ultra Series Centrifuge (Thermo Scientific). After centrifugation, fractions were collected using a BioComp Gradient Station ip. RNA content was measured at A260 concurrent with fraction collection using Triax Flow Cell v1.50A software. AUCs and analyses thereof were calculated using Prism 8 software.

After collection, fractions were prepared for RNA precipitation by adding one-tenth of fraction volume of 3 M NaOAc and 1 volume of fraction volume of isopropanol and incubated at −80°C overnight. Precipitated RNAs were extracted and purified using the Direct-zol RNA Miniprep kit and protocol (Zymo Research, R2050). After adding ERCC spike-ins (Thermo Fisher 4456740) per same volume of RNA for all samples (input and fractions) to be able to normalize for potential differences in efficiency of RT or qPCR amplification, we used equal volumes of samples for RT and qPCR. For MYC, we generated a standard curve using *MYC* dsDNA amplicons at 10^3 to 10^8 absolute copy number per well. Details about primers used are included in table S8.

For WB analysis, fractions were prepared for protein precipitation by adding cold trichloroacetic acid (TCA) at 15% final and incubated at −20°C overnight. Samples were thawed on ice and centrifuged for 30 min at 15,000*g*, 4°C. Pellet was resuspended in 1 ml of cold 15% TCA to fully remove sucrose and salt and centrifuged again for 15 min at 15,000*g*, 4°C. The pellet was washed twice with 500 μl acetone and centrifuged for 10 min at 15,000*g*, 4°C. Samples were then dried using speedvac and resuspended in 1X LDS (Thermo Fisher B0007) diluted in RIPA buffer [50mM HEPES pH 7.4, 150 mM NaCl, 1% sodium deoxycholate, 0.1% SDS, 10 mM sodium pyrophosphate, 10 mM b-glycerophosphate, 1% NP-40, supplemented with 1 mM $MgCl_2$, phosphatase inhibitor cantharidin (Gold Biotechnology C-975–500), benzonase (EMD Millipore 71205–3)] and protease inhibitor cocktail as follows: 115 mM sodium molybdate dihydrate (Gold Biotechnology M-781–100), 100 mM sodium orthovanadate (Gold Biotechnology S-930–25), 100 mM sodium fluoride (Alfa Aesar AAA1301930), 200 mM imidazole (Gold Biotechnology I-902–25), and 400 mM sodium tartrate dihydrate (Alpha Aesar

AAA1618730). Samples were then boiled at 75°C for 15 min and analyzed by Western blot.

UV cross-linking and immunoprecipitation (CLIP) and RNA radiolabeling

Immunoprecipitation and radiolabeling of RNAs bound to V5-tagged proteins were performed as previously described (75) with the following modifications: 20 million cells were seeded 24 hours prior to cross-linking. Cells were centrifuged at 300*g* for 5 min, washed in 10 ml of 0.22 mm filtered media, then centrifuged again and resuspended at a final concentration of 4 million cells per ml in 0.22 μm filtered media. Cells were then cross-linked with 150 mJ/cm^2 at 254 nm using a 254 nm UV cross-linker instrument (HL-2000 HybriLinker, UVP) and centrifuged, and pellets snap frozen on dry ice.

Cross-linked cell pellets were resuspended in cold lysis buffer: 50 mM Tris-HCl pH 7.5, 300 mM NaCl, 0.5% Nonidet-P40 (IGEPAL CA-630), supplemented with complete EDTA-free protease inhibitor (1 tablet per 25 ml, Roche 11873580001) and 1X phosphatase inhibitor (100X Halt cocktail, Thermo 8440) prior to use. Cells in lysis buffer were sonicated using a Branson Digital Sonifier Model 450 fitted with 3.125-mm tapered micro tip probe on ice at 10% amplitude (2-s ON, 10-s OFF cycle, total 30 s). A Western blot was performed on lysate aliquots to quantify the levels of V5-tagged proteins. Western blot lysates were first treated with 5 U/ml RNaseI for 10 min at 37°C to completely digest RNA. Cell lysates were normalized according to the levels of V5-tagged proteins. DNase I (0.002 U/μl; Thermo Scientific EN0521) and RNase I (0.02 U/ml; Thermo Scientific AM2294) were used to digest DNA and RNA in the cell lysate for 3 min at 37°C.

Anti-V5 antibody (2.5 μg; mouse, Abcam 27671, dilution 1:2500) was used for immunoprecipitation (IP) of cross-linked RNA-protein complexes per sample. V5 antibodies were first bound to Pierce Protein A/G Magnetic Beads (Thermo Scientific 88802) in lysis buffer for 1 hour at 4°C. IP was performed in lysis buffer at 4°C overnight. As previously described (75), bound RNA-protein complexes were washed twice with stringent high-salt buffer (50 mM Tris-HCl pH 7.4, 1 M NaCl, 1 mM EDTA, 1% NP-40, 0.1% SDS, 0.5% sodium deoxycholate) and twice with low-salt buffer (20 mM Tris-HCl pH 7.4, 10 mM $MgCl_2$, 0.2% Tween-20). Half the IP lysate was used for Western blot to verify levels of V5-tagged proteins (anti-V5, Sigma V8137, dilution 1:2000). Western blot lysates were treated with 0.2 U/ml RNaseI for 10 min at 37°C to completely digest RNA. In the remaining half of the IP lysate, RNA bound to pulled down proteins was labeled with 0.25 U/μl T4 PNK (New England Biolabs M0201) and 0.25 μCi/μl [γ-32P]-ATP (Perkin Elmer BLU002Z500UC). RNA-protein complexes were eluted from the beads in 1X NuPage LDS Sample Buffer (Invitrogen NP0008) plus 10 mM DTT and run on an SDS-PAGE gel, before transfer onto a nitrocellulose membrane. The membrane was then exposed using autoradiograph film.

RNA−, RIP−, and BCR-sequencing sample preparation

RNA was extracted using TRIzol as described above, quantified with Qubit, and analyzed for integrity using RNA Pico Chips (Agilent 5067–1513) on an Agilent 2100 Bioanalyzer (Agilent Technologies). Samples with RNA integrity number (RIN) ≥ 8 were further

processed. On the basis of the available amount, 2 to 100 ng RNA was used for cDNA synthesis and qRT-PCR to validate samples identity pre-library preparation. Equal amounts of RNA were used for all samples for each experiment for library preparation. Libraries were validated on the Agilent 2100 Bioanalyzer before sequencing and quantified using Quant-iT dsDNA HS Assay (Thermo Fisher Q33120). Each library was generated with a unique index sequence, and libraries were pooled with the same ratio for all samples for sequencing, except for the RIP as described below. Library preparation, sequencing and postprocessing of raw data was performed at the Epigenomics Core and Genomics Resources Core facilities (WCM).

For SU-DHL4 RNA-seq, three independent stable lines were freshly generated as described above, selected with 1 μg/ml puromycin for 4 days, enriched for viable cells by gradient separation (Fico/Lite-LymphoH, R&D Systems I40150), and 200,000 viable cells were used for RNA extraction. For library preparation, 200 ng RNA per sample was used.

For GC B cell bulk RNA-seq, live $B220^{+}FAS^{+}$ $GL7^{+}$ cells were sorted from $B220^{+}$ enriched splenocytes on BD Influx as described above, from four CRE and five Q36H mice. Per sample, 123,000 to 344,000 GC B cells were sorted, of which 120 to 236 ng RNA was extracted.

For both SU-DHL4 and GC B cell bulk RNA-seq, libraries were prepared using Illumina TruSeq stranded-mRNA sample kit and subjected to single read 50 bp sequencing on an Illumina HiSeq 2500.

For Myc^{GFP+} and Myc^{GFP-} GC B cells RNA-seq, live $B220^{+}FAS^{+}CD38^{-}$ Myc^{GFP+} or Myc^{GFP-} cells were sorted from $B220^{+}$ enriched splenocytes on BD Influx as described above, from two CRE and three Q36H mice. Per sample, 4000 to 8850 Myc^{GFP+} GC B cells and 155,000 to 250,000 Myc^{GFP-} GC B cells were sorted, of which 1.9 to 3.8 ng (Myc^{GFP+}) and 60 to 300 ng (Myc^{GFP-}) RNA was extracted. Eleven PCR cycles and 0.95 ng RNA were used for all samples for library preparation using the Ultra-low input RNA kit (Takara SMART-Seq v4), and samples were subjected to single read 50 bp sequencing on an Illumina HiSeq.

For Bcl2+Q36H and Bcl2 lymphoma B cells RNA-seq, 300,000 GC B cells from Bcl2 and Bcl2+Q36H mice were sorted as live $B220^{+}$ $FAS^{+}GL7^{+}$ cells from PNA^{+} enriched splenocytes on BD Influx or BD FACSAria II at 8 months after transplantation. Per sample, 150 ng RNA was used for library preparation using Illumina TruSeq stranded-mRNA sample kit followed by single read 50 bp sequencing on an Illumina HiSeq.

For SU-DHL4 RIP-sequencing, input and RIP RNAs were obtained from two independently generated stable lines, each RIPed in duplicates from 35 million cells each as described above. We recovered ~7 to 14 μg RNA from input samples and 500 to 1700 ng RNA from RIP samples. We added ERCC RNA spike-ins (Thermo Fisher 4456740) per same volume of RNA for all input or for all RIP samples to be able to normalize for possible global changes in starting RNA amount and pull down RNA amount between samples. Of these, we used 250 ng RNA in 50 μl for each of the input and RIP samples for library preparation using TruSeq-stranded-mRNA sample kit. We used 22 nmol library for all input and RIP

samples, except for the EGFP-V5 RIP samples, for which we added a maximum of 11 nmol each (2:1 ratio, normalized during analysis). Samples were subjected to paired-end 50 bp sequencing on a NovaSeq SP at 700 million reads to achieve 29 million reads per sample.

For BCR sequencing analysis, we used remaining splenocytes from Bcl2 and Bcl2+Q36H mice at 8 months after transplantation that were not used for PNA enrichment and GC B cells sorting, had been treated with red blood cell lysis solution (QIAGEN 158904), and viably frozen in FBS with 10% DMSO. We thawed these splenocytes and extracted gDNA using Puregene Gentra cell kit (QIAGEN 158388). gDNA (1.5 μg) was sent to Adaptive Bio-technologies for ImmunoSeq assay to sequence a 125-bp-long VDJ region around the IgH complementarity-determining region 3 (CDR3; see fig. S16B). Briefly, the somatically rearranged IgH CDR3 was amplified using a two-step amplification, bias-controlled multiplex PCR approach (76). The first PCR consisted of forward and reverse amplification primers specific for every V and J gene segment and amplified the hypervariable CDR3 of the immune receptor locus. The second PCR added a proprietary barcode sequence and Illumina adapter sequences.

RNA-sequencing analysis

For all RNA-seq analyses, results were aligned to mm10 or hg19 using STAR (77) and annotated to RefSeq using the Rsubread package (78). Differential expression was called using edgeR generalized linear model with TMM normalization (79, 80) with thresholds of FC >1.5 and Benjamini-Hochberg corrected $P < 0.01$. Murine Bcl2 and Bcl2+Q236H tumors were additionally modeled using a batch correction for the respective cell sorter and, because of sex imbalance between conditions, only autosomal genes were used for analysis.

Gene set enrichment was assessed using the GSEA algorithm, a computational method based on the Kolmogorov-Smirnov test (34). GSEA network analysis was performed by running GSEA using the Hallmark and Canonical Pathways gene sets from MSigDB. Jaccard similarity index was calculated for all pairs of leading-edge genes from significantly enriched signatures (FDR < 0.05; table S3). Network was then generated using the R igraph package (81), adjusting size of node for degree of connectivity.

Unsupervised pathway analysis was performed using information-theoretic pathway analysis approach as described previously (82). Briefly, pathways that are informative about nonoverlapping gene groups were identified. Pathways annotations were used from the Biological Process annotations of the Gene Ontology database (http://www.geneontology.org), Human Protein Reference Database (http://www.hprd.org), MSigDB C2 (http://www.gsea-msigdb.org/gsea/msigdb/human/genesets.jsp?collection=C2), and signature categories from the Staudt Lab Signature database (83). Only human-curated annotations were used from the Gene Ontology database, and only pathways with five genes or more, and with 300 genes or less were evaluated. This pathway analysis estimates how informative each pathway is about the target gene groups and applies a randomization-based statistical test to assess the significance of the highest information values. We used the default significance threshold of $P < 0.005$. We estimated the FDR by randomizing the input profiles iteratively on shuffled profiles with identical parameters and thresholds, finding that the FDR was always lower than 5%. For each informative pathway, we determined

the extent to which the pathway was over-represented in the target gene group, using the hypergeometric distribution, as described previously (82).

Unsupervised hierarchical clustering was performed on RNA-seq using most variable genes (95th percentile for standard deviation across all samples). Euclidean distance was calculated using log-transformed expression values for GC B cell RNA-seq from CRE and Q36H samples [log(TPM+0.1)] and log-transformed FPKM expression values adjusted for sorter batch effect using the ComBat function of the R package sva (84, 85) with parametric empirical Bayes adjustment for the Bcl2 and Bcl2 +Q36H lymphoma RNA-seq. Hierarchical clustering was then performed using Ward's minimum variance method.

Motif analysis

HOCOMOCO (v11) motifs (86) were assessed for enrichment in gene promoter (TSS ± 2kb) using CentriMO tool from the MEME framework (87, 88). Comparative enrichment was evaluated within genes found unregulated in $BTG1^{Q36H}$ versus genes that were expressed in SU-DHL4 cells (FPKM > 0.1) and were non-differentially expressed. We performed exact test to evaluate the significance of the number of best matches in the region in the primary set compared with the number of best matches in the same region in the control set of sequences.

RIP sequencing analysis

RIP sequencing results were aligned to a merged hg19-ERCC genome using STAR and annotated to RefSeq using the Rsubread package. Read counts between samples were normalized to ERCC spike-ins using the RUVg method (89). Differential RIP abundance was called by a linear additive model using edgeR, adjusting for ERCC spike-ins and subtracting input transcript level. Transcripts found to be lost in $BTG1^{Q36H}$ versus $BTG1^{WT}$ pull-downs were filtered to remove any transcripts that were present less than twofold in $BTG1^{WT}$ RIP versus input.

Targeted single-cell RNA sequencing

We sorted competing Q36H (CD45.1/2) and CREneg control (CD45.1) GC B cells ($DAPI^-B220^+CD4^-FAS^+CD38^-$) as well as T_{FH} cells ($DAPI^-B220^-CD4^+CXCR5^{hi}$ $PD\text{-}1^{hi}$) from $n = 4$ mice on a BD Influx sorter as described above. Samples were tagged, counted, and multiplexed into three replicates at a Q36H: CREneg:TFH ratio of 60:28:12. BD Rhapsody data were generated according to the manufacturer's protocol. Briefly, a total of 25,000 to 30,000 cells was loaded per BD Rhapsody Cartridge, into two cartridges for single-cell capture, followed by reverse transcription and exonuclease I treatment, library preparation, and sequencing on a NextSeq500, using 75 bp paired-end sequencing. The targeted panel of $n = 496$ genes (table S7) comprised BD Rhapsody mouse immune response panel (BD 633753, $n = 397$) plus a custom set of genes implicated in GC or lymphoma biology ($n = 99$) designed with help from BD. Fastq files were uploaded to Seven Bridges Genomics. Data were demultiplexed and sequences were analyzed with BD's Rhapsody pipeline (BD Rhapsody Analysis Pipeline 1.4 Beta) on Seven Bridges (www.sevenbridges.com). This pipeline included RSEC and DBEC filtration of UMI counts and generated a sparse matrix

file of features by barcodes. This sparse matrix data were read into R using the R package Seurat v3.0.2 (90). Data were then scaled and log normalized.

We focused on GC B cell clusters for downstream analysis, on the basis of *Cd19* expression and absence of *Cd4* or *Cd8* expression. Linear dimensional reduction was performed by calculation of PCA from the most variable genes. Cells were then clustered using a resolution value of 0.5 and visualized by UMAP determined from dims 1:10. Module scores were calculated using the AddModuleScore function with a control value of 5. Individual genes and module scores were projected and used for appropriate classification of clusters. Single cells were assigned to populations (DZ, LZ, or LZ-to-DZ recycling) on the basis of high score of gene markers and module scores per cluster.

Single-cell trajectory analysis

Cell cycle phase identities were assigned by the Seurat CellCycleScoring function. RNA trajectory analysis was performed using the R package Slingshot v1.2.0 (91). This package was used to create a "pseudotime" based on a combination of PCAs 1 and 2 calculated by Seurat, using cells identified as S phase cells as the anchor point. Cells that belonged to a pre-memory B cell cluster on the basis of *Cd38* expression were excluded, and lineage plots were generated by projecting pseudotime onto cells mapped by PCAs 1 and 2. Pseudotime density plots were generated using cell cycle phase identity and the ggplot2 v3.2.1 geom_ density function. The difference in density between genotypes was determined by using the density function in R on the pseudotime density plot for each genotype and subtracting the CREneg density Y values from the Q36H density Y values. These differences were then plotted by ggplot2 geom_col function. Difference in density distribution was tested by Wilcoxon rank sum test on the pseudotime values for each genotype. Scatterplots were created by plotting pseudotime on the *x* axis and module scores on the *y* axis. Average score and confidence interval per genotype were plotted with the geom_smooth function.

WGS driver analysis

Whole-genome sequencing (WGS) alignments for 101 DLBCL and matched normal sample pairs were retrieved as hg19-aligned BAM files from the European Genome Archive (https://ega-archive.org/, EGAD00001002123) and stripped of alignment information via Picard tools RevertSam, according to GATK best practices (https://software.broadinstitute.org/gatk/best-practices) to generate unmapped BAM files. The unmapped BAM files subsequently underwent alignment to hg38 and somatic variant calling for SNVs, indels, and structural variants (SVs) via the Sarek pipeline v2.5.1 (https://github.com/nf-core/sarek). Briefly, the Sarek pipeline (92) applies BWA mem alignment, duplicate removal, base recalibration, somatic SNV/indel calling via Strelka2 (93), somatic SV calling via Manta (94), and variant annotation with VEP (95). In summary, this pipeline yielded VCF files containing 1.36 million SNVs across 101 DLBCL cases, which were used for downstream analyses.

FishHook (https://github.com/mskilab/fishHook) was used to model background mutational processes and nominate DLBCL mutational hotspots across the cohort of 101 DLBCL cases (see above). FishHook takes as input mutation calls (e.g., VCF), a set of hypothesis intervals (.bed files), an eligible territory (.bed file), and a set of genomic covariates (.bed, .bw files)

and outputs a model of mutation density and hypothesis intervals associated with a *P* value and enrichment score. Briefly, fishHook (96) models genome-wide somatic mutation density in tumor genomes across the intersection of an eligible territory (e.g., coding sequences, mappable genomic regions) and set of hypothesis intervals (e.g., genes) as a function of genomic covariates, which can represent sequence context composition, chromatin features, or the fractional overlap with reference genomic annotations. The maximum likelihood fit of a fishHook model, implemented as a gamma-Poisson regression, assigns weights to covariates and an expected mutation density to each hypothesis interval. An enrichment value is computed at each hypothesis interval as the ratio of observed to expected mutation density. The model is further used to define a cumulative distribution function (CDF) for mutation density at each interval. Each interval is then assigned a one-sided *P* value as the probability that the mutation density is greater or equal than the observed density.

FishHook was applied to analyze the distribution of 1.36M DLBCL SNVs across 24,498 protein coding genes (GRCh38) using coding sequences as the eligible territory a set of genomic covariates representing B cell–specific transcriptional and chromatin state. To generate the set of covariates, we annotated .bed files of protein coding genes with the number of ATAC-seq peaks from human purified GC B cells (unpublished data) within 100 kb, the number of GC B cell H3K27ac ChIP-seq defined super-enhancers within 100 kb, and the number of TSS within 100 kb for genes expressed >1 TPM in human GC B cells (RNA-seq). Super-enhancers were called from previously reported H3K27ac ChIP-seq data from human purified GC B cells (97) using the ROSE method (98).The resulting fishHook model with three covariates was fit to annotate genes with *P* values and enrichment scores (table S1). We labeled genes with (Benjamini-Hochberg) FDR < 0.01 as significant. We generated Q-Q plots by pairing observed −log10 transformed quantiles of observed *P* values (*y* axis) with their corresponding −log10 transformed quantiles from the uniform distribution (*x* axis). A genomic inflation factor λ was computed as the slope of a least-squares regression line fitting these data while intercepting the origin. The value of λ (<1.05) was consistent with minimal statistical inflation (99).

BCR sequencing analysis

Initial immunoSeq BCR sequencing data processing was performed using the immunoSeq Analyzer 3.0 (Adaptive Biotechnologies). Only sequences associated with at least five templates were retained for further analysis. BCR repertoire sequencing data was then analyzed using the Immcantation (www.immcantation.org) framework. VDJ genes for each sequence were aligned to the IMGT GENE-DB database accessed 22 June 2021 (100) using IgBlast v1.17.1 (101) and Change-O v1.1.0 (102). Only IMGT V-gene sequences obtained from C57BL/6 mice were included in the reference database. Nonproductive BCRs were removed. Sequences were grouped into clonal clusters, which contain B cells that relate to each other by somatic hypermutations from a common VDJ ancestor. Sequences were first grouped by common IGHV gene annotations, IGHJ gene annotations, and junction lengths. Using the hierarchicalClones function of *scoper* v1.2.0 (103), sequences within these groups differing by a length normalized Hamming distance of 0.1 within the CDR3 region were defined as clones using single-linkage hierarchical clustering (104). This threshold was determined through manual inspection of distance to nearest neighbor plots using shazam

v1.1.0 (105). Within each clone, germline sequences were reconstructed with D segment and N/P regions masked (replaced with “N” nucleotides) using the createGermlines function within *dowser* (106).

Somatic hypermutation was calculated as the Hamming distance between each sequence and its predicted unmutated germline ancestor. Because immunoSEQ data contains only the partial V-gene sequence, only between 69 and 108 nucleotides of region FWR3 were used in this calculation. To quantify B cell clonal diversity, we calculated Simpson’s diversity for each sample using the alphaDiversity function of *alakazam* v1.2.0 (102). Lower values of Simpson’s diversity indicate a greater probability of two random sequences belonging to the same clone, consistent with more large clones. To account for differences in sequence depth, samples within each comparison were down sampled to the same number of sequences, and the mean of 1000 such resampling repetitions was reported. Samples with fewer than 30 sequences were excluded. Clonal lineage trees were built using *dowser* v1.0.0 (106) and IgPhyML v1.1.4 (50). Because predicted germline junction sequences are masked, only V-gene sites were used to build lineage trees and estimate substitution model parameters. Codons split by insertions relative to the IMGT germline reference sequences were masked using the maskSequences function in *dowser*. Lineage tree topologies, branch lengths, and subject-wide substitution model parameters using maximum likelihood under the GY94 model (107). Using fixed tree to-pologies estimated from the GY94 model, we then estimated branch lengths and subject-wide parameter values under the HLP19 model (50). Only clones containing at least two unique sequences and a total >100 sequence reads were included. Trees were visualized using *dowser* and *ggtree* v3.3.1.901 (108).

In silico GC modeling

An agent-based GC model with molecular events of GC B cell selection based on DisseD theory (47) was used to perform in silico simulations. The model uses elements described before (109–111) and differential equations describing evolution of the signaling molecules mTOR, Myc, and FoxO. A three-dimensional lattice with chemokine gradients is used to represent the GC area and incorporates randomly distributed T_{FH} cells and follicular dendritic cells. Founder GC B cells enter the GC area with a fixed rate for an initial time period, undergo six divisions, and eventually acquire a LZ phenotype. LZ B cells interact with follicular dendritic cells, resulting in the acquisition of antigen with an affinity-based probability. A four-dimensional shape space (112) is used to represent the B cell affinity, where the position of a B cell with respect to a predefined optimal position denoting the antigen corresponds to the affinity of the cell. Successful antigen collection is followed by interactions with T_{FH} cells. When multiple B cells are bound to the same T_{FH} cell, the T_{FH} cell polarizes toward and signals the B cell with the highest amount of antigen collected. Acquisition of antigen and interaction with T_{FH} cell induces changes in the levels of mTOR, Myc, and FoxO molecules. Time period of interaction with follicular dendritic cells and T_{FH} cells ends, and a fate decision is initiated, either at the time when mTOR reaches a threshold value or when the time exceeds a maximum time period of 18 hours. GC B cells with Myc and mTOR levels reaching predefined threshold values are selected. Selected cells return to the DZ phenotype and divide a certain number of times, as determined by Myc levels at the

time of selection by T_{FH} cells. Detailed description of the GC model and parameter values are provided in the supplementary text of (47).

Two models were considered to recapture the behavior of BTG1 mutant GC B cells. In the first model, we considered a faster up-regulation of mTOR and Myc: The rate of mTOR and Myc up-regulation in Btg1 mutant GC B cells upon contact with TFH cells was increased 1.12 times as compared with WT cells. In the second model, we considered a faster up-regulation of mTOR and Myc, coupled with a shorter S phase duration: In addition to the 1.12 times faster up-regulation of mTOR and Myc, Btg1 mutant GC B cells were assumed to undergo accelerated S phase progression. Average S phase duration of mutant GC B cells was shortened by 21% as compared with WT cells.

Each of the two models were tested with different simulation setups, corresponding to the competitive and noncompetitive in vivo experiments. In the competitive setup, founder GC B cells at the start of the simulation were assigned as either Btg1 mutant or WT with a probability of 0.5, for equal starting proportions of mutant and WT GC B cells. Positions of GC B cells in the shape space were chosen at a distance of 2 from the optimal position, to mimic the high affinity of $B1–8^{hi}$ cells. For the noncompetitive setup, separate simulations were performed with 100% cells being WT or Btg1 mutant GC B cells, and affinities were randomly chosen. Each simulation was repeated 300 times, and the mean and SD values were calculated. To quantify the relative difference between mutant and WT, mutant readouts were normalized with corresponding WT readouts. In vivo experimental data were normalized in a similar way for comparison to in silico simulation results. Simulations were performed with C++, and statistical tests were performed using R.

Survival analyses on human ABC-DLBCL cases

Kaplan-Meier estimator was used to estimate the overall survival probability followed by log-rank test to compare the difference between *BTG1* mutational status. Univariable and multivariable Cox regression were used to assess the overall survival difference between *BTG1* mutational status, adjusting for IPI, LymphGen call, and sex. All analyses were performed in statistical software SAS v9.4 (SAS Institute).

Statistics

For all statistical analyses, sample size (n) for each experimental group, the nature of replicates, and details for statistical tests used were specified either in the figure legend, main text, or the methods section.

Supplementary Material

Refer to Web version on PubMed Central for supplementary material.

ACKNOWLEDGMENTS

The authors thank Y. Jiang for support with conditional mouse line generation strategy; A. Intlekofer for advice and use of the Coulter counter; T. C. Lee for technical support; X. Wang and C. Meydan for data curation; J. C. Hellmuth for support in data analysis; C. Wheeler and G. Fayzikhodjaeva for support with mouse colonies management; S. Monette and M. S. Jiao from the Laboratory of Comparative Pathology (WCM/MSKCC) for support in optimizing IHC staining; C. Durmaz for support with graphical illustration; and L. Scourzic and

members of the Melnick and Victora laboratories for discussions and suggestions. The authors acknowledge the Epigenomics, Genomics Resources, Flow Cytometry, and Optical Microscopy core facilities (WCM); the Laboratory of Comparative Pathology (WCM/MSKCC); the Mouse Genetics Core Facility (MSKCC); and the David A. Cofrin Center for Biomedical Information at the HRH Prince Alwaleed Bin Talal Bin Abdulaziz Alsaud Institute for Computational Biomedicine (WCM).

Funding:

Funding was provided by ASH Fellow-to-Faculty scholar award ASHI 204241-01 (C.M.); Leukemia & Lymphoma Society Special Fellow fellowship 3384-19 (C.M.); Lymphoma Research Foundation fellowship LRF-17030307-02 (C.M.); ASH Research Restart award (C.M.); Lymphoma Research Foundation fellowship LSRMP-817214 (C.M.); Damon Runyon Cancer Research Foundation, Berger Foundation fellowship DRG-2353-19 (J.P.); NIH NCI award 1F31CA254302-01 (C.R.C.); COSMIC Marie Skłodowska-Curie grant 765158 (T.A.); a Swiss National Science Foundation fellowship (D.B.); a National Cancer Center postdoctoral fellowship (D.B.); NIH NCI K99CA212276 (D.B.); AACR-Incyte Lymphoma Research Fellowship 21-40-46-PAPI (A.P.); NIH NIAID grant R01AI104739 (K.B.H.); a Cancer Research Institute Irvington postdoctoral fellowship (J.E.); an Agency for Science, Technology and Research (A*STAR) award (H.X.P.); NIH NCI award 1F31CA257204-01A1 (C.M.E.); Lymphoma Research Foundation fellowship 817442 (H.M.I.); NIH NCI award T32CA062948 (H.M.I.); Deutsche Forschungsgemeinschaft PE3140/1-1 (B.P.); Deutsche Krebshilfe, grant Mildred Scheel Nachwuchszentrum 70113307 (B.P.); NIH NCI award 1F31CA220981-01 (A.S.D.); ASH Scholar Award FP00000270 (D.T.T.N.); NIH grant UL1TR002384 (O.E.); NIH grant R01CA194547 (O.E.); Leukemia & Lymphoma Society SCOR grants 180078-02 and 7021-20 (O.E.); a Leukemia & Lymphoma Society Scholarship (M.G.K.); an MSK Lymphoma SPORE grant (M.G.K.); NIH grant R01CA186702 (S.R.J.); a Michael Smith Foundation for Health Research Health Professional Investigator Award (D.W.S.); 1923 Fund (G.K.); NIH grant R01AI139117 (G.D.V.); The Starr Foundation Tri-Institutional Stem Cell Initiative 2021-033 (M.G.K. and A.M.); Starr Cancer Consortium grant I11-0027 (O.E., G.D.V., and A.M.); NIH NCI grant R35CA220499 (A.M.); Leukemia & Lymphoma Society TRP grant 6572 (A.M.); Leukemia & Lymphoma Society SCOR grant 7012 (A.M.); the Follicular Lymphoma Consortium (A.M.); and the Samuel Waxman Cancer Research Foundation (AM).

Competing interests:

The authors declare no direct competing financial or nonfinancial interests. K.B.H. receives consulting fees from Prellis Biologics. A.C. is on the immunohistochemistry advisory board for Leica Biosystems and consults for Boehringer Ingelheim Pharmaceuticals. O.E. is supported by Janssen, Johnson and Johnson, Volastra Therapeutics, AstraZeneca, and Eli Lilly research grants; is a scientific adviser to and equity holder in Freenome, Owkin, Volastra Therapeutics, and OneThree Biotech; and consults for and advises Champions Oncology. M.G.K. discloses provision of services with 28-7 Therapeutics (uncompensated), Accent Therapeutics, AstraZeneca, and Kumquat Biosciences; and is a scientific adviser to and equity holder in 858 Therapeutics. S.R.J. is scientific founder of, adviser to, and owns equity in Gotham Therapeutics and 858 Therapeutics. D.W.S. receives research funding from Janssen and NanoString; has consulted for Abbvie, AstraZeneca, Celgene, and Janssen; and was named inventor on patents describing the use of gene expression in subtyping lymphomas. G.D.V. is a scientific adviser for Vaccine Company, Inc. A.M. receives research funding from Janssen Pharmaceuticals, Sanofi, Epizyme, and Daiichi Sankyo; has consulted for Epizyme and Constellation; and is on the advisory board of KDAC Pharma.

Data and materials availability:

All data are available in the manuscript or the supplementary materials or are deposited as follows: sequencing data generated for this study is available on NCBI Gene Expression Omnibus (GEO) under accession number GSE167786 and codes and mathematical algorithms used in this study are accessible on Zenodo (113).

REFERENCES AND NOTES

1. Mesin L, Ersching J, Victora GD, Germinal center B cell dynamics. Immunity 45, 471–482 (2016). doi: 10.1016/j.immuni.2016.09.001 [PubMed: 27653600]
2. Nakagawa R et al. , Permissive selection followed by affinity-based proliferation of GC light zone B cells dictates cell fate and ensures clonal breadth. Proc. Natl. Acad. Sci. U.S.A 118, e2016425118 (2021). doi: 10.1073/pnas.2016425118
3. Dominguez-Sola D et al. , The proto-oncogene *MYC* is required for selection in the germinal center and cyclic reentry. Nat. Immunol 13, 1083–1091 (2012). doi: 10.1038/ni.2428 [PubMed: 23001145]

4. Calado DP et al. , The cell-cycle regulator c-Myc is essential for the formation and maintenance of germinal centers. Nat. Immunol 13, 1092–1100 (2012). doi: 10.1038/ni.2418 [PubMed: 23001146]
5. Ersching J et al. , Germinal center selection and affinity maturation require dynamic regulation of mTORC1 kinase. Immunity 46, 1045–1058.e6 (2017). doi: 10.1016/j.immuni.2017.06.005 [PubMed: 28636954]
6. Mlynarczyk C, Fontán L, Melnick A, Germinal center-derived lymphomas: The darkest side of humoral immunity. Immunol. Rev 288, 214–239 (2019). doi: 10.1111/imr.12755 [PubMed: 30874354]
7. Pasqualucci L, Molecular pathogenesis of germinal center-derived B cell lymphomas. Immunol. Rev 288, 240–261 (2019). doi: 10.1111/imr.12745 [PubMed: 30874347]
8. Alizadeh AA et al. , Distinct types of diffuse large B-cell lymphoma identified by gene expression profiling. Nature 403, 503–511 (2000). doi: 10.1038/35000501 [PubMed: 10676951]
9. Schmitz R et al. , Genetics and pathogenesis of diffuse large B-cell lymphoma. N. Engl. J. Med 378, 1396–1407 (2018). doi: 10.1056/NEJMoa1801445 [PubMed: 29641966]
10. Chapuy B et al. , Molecular subtypes of diffuse large B cell lymphoma are associated with distinct pathogenic mechanisms and outcomes. Nat. Med 24, 679–690 (2018). doi: 10.1038/s41591-018-0016-8 [PubMed: 29713087]
11. Wright GW et al. , A probabilistic classification tool for genetic subtypes of diffuse large B cell lymphoma with therapeutic implications. Cancer Cell 37, 551–568.e14 (2020). doi: 10.1016/j.ccell.2020.03.015 [PubMed: 32289277]
12. Venturutti L et al. , TBL1XR1 mutations drive extranodal lymphoma by inducing a pro-tumorigenic memory fate. Cell 182, 297–316.e27 (2020). doi: 10.1016/j.cell.2020.05.049 [PubMed: 32619424]
13. Venturutti L et al. , An aged/autoimmune B-cell program defines the early transformation of extranodal lymphomas. Cancer Discov.OF1–OF28 (2022). doi: 10.1158/2159-8290.CD-22-0561
14. Lin WJ, Gary JD, Yang MC, Clarke S, Herschman HR, The mammalian immediate-early TIS21 protein and the leukemia-associated BTG1 protein interact with a protein-arginine *N*-methyltransferase. J. Biol. Chem 271, 15034–15044 (1996). doi: 10.1074/jbc.271.25.15034 [PubMed: 8663146]
15. Rouault JP et al. , Interaction of BTG1 and p53-regulated BTG2 gene products with mCaf1, the murine homolog of a component of the yeast CCR4 transcriptional regulatory complex. J. Biol. Chem 273, 22563–22569 (1998). doi: 10.1074/jbc.273.35.22563 [PubMed: 9712883]
16. Prévôt D et al. , The leukemia-associated protein Btg1 and the p53-regulated protein Btg2 interact with the homeoprotein Hoxb9 and enhance its transcriptional activation. J. Biol. Chem 275, 147–153 (2000). doi: 10.1074/jbc.275.1.147 [PubMed: 10617598]
17. Busson M et al. , Coactivation of nuclear receptors and myogenic factors induces the major BTG1 influence on muscle differentiation. Oncogene 24, 1698–1710 (2005). doi: 10.1038/sj.onc.1208373 [PubMed: 15674337]
18. Hata K, Nishijima K, Mizuguchi J, Role for Btg1 and Btg2 in growth arrest of WEHI-231 cells through arginine methylation following membrane immunoglobulin engagement. Exp. Cell Res 313, 2356–2366 (2007). doi: 10.1016/j.yexcr.2007.03.021 [PubMed: 17466295]
19. Tijchon E et al. , Tumor suppressors BTG1 and BTG2 regulate early mouse B-cell development. Haematologica 101, e272–e276 (2016). doi: 10.3324/haematol.2015.139675 [PubMed: 27036158]
20. Almasmoum HA, Airhihen B, Seedhouse C, Winkler GS, Frequent loss of BTG1 activity and impaired interactions with the Caf1 subunit of the Ccr4-Not deadenylase in non-Hodgkin lymphoma. Leuk. Lymphoma 62, 281–290 (2021). doi: 10.1080/10428194.2020.1827243 [PubMed: 33021411]
21. Kotlov N et al. , Clinical and biological subtypes of B-cell lymphoma revealed by microenvironmental signatures. Cancer Discov. 11, 1468–1489 (2021). doi: 10.1158/2159-8290.CD-20-0839 [PubMed: 33541860]
22. Ma MCJ et al. , Subtype-specific and co-occurring genetic alterations in B-cell non-Hodgkin lymphoma. Haematologica 107, 690–701 (2022). doi: 10.3324/haematol.2020.274258 [PubMed: 33792219]

23. Ennishi D et al. , *TMEM30A* loss-of-function mutations drive lymphomagenesis and confer therapeutically exploitable vulnerability in B-cell lymphoma. Nat. Med 26, 577–588 (2020). doi: 10.1038/s41591-020-0757-z [PubMed: 32094924]
24. Reddy A et al. , Genetic and functional drivers of diffuse large B cell lymphoma. Cell 171, 481–494.e15 (2017). doi: 10.1016/j.cell.2017.09.027 [PubMed: 28985567]
25. Zhang J et al. , Genetic heterogeneity of diffuse large B-cell lymphoma. Proc. Natl. Acad. Sci. U.S.A 110, 1398–1403 (2013). doi: 10.1073/pnas.1205299110 [PubMed: 23292937]
26. Lohr JG et al. , Discovery and prioritization of somatic mutations in diffuse large B-cell lymphoma (DLBCL) by whole-exome sequencing. Proc. Natl. Acad. Sci. U.S.A 109, 3879–3884 (2012). doi: 10.1073/pnas.1121343109 [PubMed: 22343534]
27. Morin RD et al. , Frequent mutation of histone-modifying genes in non-Hodgkin lymphoma. Nature 476, 298–303 (2011). doi: 10.1038/nature10351 [PubMed: 21796119]
28. Cerami E et al. , The cBio cancer genomics portal: An open platform for exploring multidimensional cancer genomics data. Cancer Discov. 2, 401–404 (2012). doi: 10.1158/2159-8290.CD-12-0095 [PubMed: 22588877]
29. Gao J et al. , Integrative analysis of complex cancer genomics and clinical profiles using the cBioPortal. Sci. Signal 6, pl1 (2013). doi: 10.1126/scisignal.2004088 [PubMed: 23550210]
30. Rodier A et al. , Identification of functional domains involved in BTG1 cell localization. Oncogene 20, 2691–2703 (2001). doi: 10.1038/sj.onc.1204398 [PubMed: 11420681]
31. Kots E, Mlynarczyk C, Melnick A, Khelashvili G, Conformational transitions in BTG1 antiproliferative protein and their modulation by disease mutants. Biophys. J 121, 3753–3764 (2022). doi: 10.1016/j.bpj.2022.04.023 [PubMed: 35459639]
32. Rickert RC, Roes J, Rajewsky K, B lymphocyte-specific, Cre-mediated mutagenesis in mice. Nucleic Acids Res. 25, 1317–1318 (1997). doi: 10.1093/nar/25.6.1317 [PubMed: 9092650]
33. Shih TA, Roederer M, Nussenzweig MC, Role of antigen receptor affinity in T cell–independent antibody responses *in vivo*. Nat. Immunol 3, 399–406 (2002). doi: 10.1038/ni776 [PubMed: 11896394]
34. Subramanian A et al. , Gene set enrichment analysis: A knowledge-based approach for interpreting genome-wide expression profiles. Proc. Natl. Acad. Sci. U.S.A 102, 15545–15550 (2005). doi: 10.1073/pnas.0506580102 [PubMed: 16199517]
35. Liberzon A et al. , Molecular signatures database (MSigDB) 3.0. Bioinformatics 27, 1739–1740 (2011). doi: 10.1093/bioinformatics/btr260 [PubMed: 21546393]
36. Liberzon A et al. , The Molecular Signatures Database (MSigDB) hallmark gene set collection. Cell Syst. 1, 417–425 (2015). doi: 10.1016/j.cels.2015.12.004 [PubMed: 26771021]
37. Huang CY, Bredemeyer AL, Walker LM, Bassing CH, Sleckman BP, Dynamic regulation of *c-Myc* proto-oncogene expression during lymphocyte development revealed by a *GFP-c-Myc* knock-in mouse. Eur. J. Immunol 38, 342–349 (2008). doi: 10.1002/eji.200737972 [PubMed: 18196519]
38. Casola S et al. , Tracking germinal center B cells expressing germ-line immunoglobulin g1 transcripts by conditional gene targeting. Proc. Natl. Acad. Sci. U.S.A 103, 7396–7401 (2006). doi: 10.1073/pnas.0602353103 [PubMed: 16651521]
39. Tesi A et al. , An early Myc-dependent transcriptional program orchestrates cell growth during B-cell activation. EMBO Rep. 20, e47987 (2019). doi: 10.15252/embr.201947987 [PubMed: 31334602]
40. Luo EC et al. , Large-scale tethered function assays identify factors that regulate mRNA stability and translation. Nat. Struct. Mol. Biol 27, 989–1000 (2020). doi: 10.1038/s41594-020-0477-6 [PubMed: 32807991]
41. Hwang SS et al. , mRNA destabilization by BTG1 and BTG2 maintains T cell quiescence. Science 367, 1255–1260 (2020). doi: 10.1126/science.aax0194 [PubMed: 32165587]
42. Li Y, Choi PS, Casey SC, Dill DL, Felsher DW, MYC through miR-17–92 suppresses specific target genes to maintain survival, autonomous proliferation, and a neoplastic state. Cancer Cell 26, 262–272 (2014). doi: 10.1016/j.ccr.2014.06.014 [PubMed: 25117713]
43. Caeser R, Gao J, Di Re M, Gong C, Hodson DJ, Genetic manipulation and immortalized culture of ex vivo primary human germinal center B cells. Nat. Protoc 16, 2499–2519 (2021). doi: 10.1038/s41596-021-00506-4 [PubMed: 33837304]

44. Victora GD et al. , Germinal center dynamics revealed by multiphoton microscopy with a photoactivatable fluorescent reporter. Cell 143, 592–605 (2010). doi: 10.1016/j.cell.2010.10.032 [PubMed: 21074050]
45. Finkin S, Hartweger H, Oliveira TY, Kara EE, Nussenzweig MC, Protein amounts of the MYC transcription factor determine germinal center B cell division capacity. Immunity 51, 324–336.e5 (2019). doi: 10.1016/j.immuni.2019.06.013 [PubMed: 31350178]
46. Gitlin AD, Shulman Z, Nussenzweig MC, Clonal selection in the germinal centre by regulated proliferation and hypermutation. Nature 509, 637–640 (2014). doi: 10.1038/nature13300 [PubMed: 24805232]
47. Meyer-Hermann M, A molecular theory of germinal center B cell selection and division. Cell Rep. 36, 109552 (2021). doi: 10.1016/j.celrep.2021.109552 [PubMed: 34433043]
48. Ogilvy S et al. , Constitutive Bcl-2 expression throughout the hematopoietic compartment affects multiple lineages and enhances progenitor cell survival. Proc. Natl. Acad. Sci. U.S.A 96, 14943–14948 (1999). doi: 10.1073/pnas.96.26.14943 [PubMed: 10611317]
49. Egle A, Harris AW, Bath ML, O'Reilly L, Cory S, VavP-*Bcl2* transgenic mice develop follicular lymphoma preceded by germinal center hyperplasia. Blood 103, 2276–2283 (2004). doi: 10.1182/blood-2003-07-2469 [PubMed: 14630790]
50. Hoehn KB et al. , Repertoire-wide phylogenetic models of B cell molecular evolution reveal evolutionary signatures of aging and vaccination. Proc. Natl. Acad. Sci. U.S.A 116, 22664–22672 (2019). doi: 10.1073/pnas.1906020116 [PubMed: 31636219]
51. Nedelcu AM, The evolution of multicellularity and cancer: Views and paradigms. Biochem. Soc. Trans 48, 1505–1518 (2020). doi: 10.1042/BST20190992 [PubMed: 32677677]
52. Baker NE, Emerging mechanisms of cell competition. Nat. Rev. Genet 21, 683–697 (2020). doi: 10.1038/s41576-020-0262-8 [PubMed: 32778819]
53. de la Cova C, Abril M, Bellosta P, Gallant P, Johnston LA, *Drosophila* myc regulates organ size by inducing cell competition. Cell 117, 107–116 (2004). doi: 10.1016/S0092-8674(04)00214-4 [PubMed: 15066286]
54. Moreno E, Basler K, dMyc transforms cells into supercompetitors. Cell 117, 117–129 (2004). doi: 10.1016/S0092-8674(04)00262-4 [PubMed: 15066287]
55. Gitlin AD et al. , T cell help controls the speed of the cell cycle in germinal center B cells. Science 349, 643–646 (2015). doi: 10.1126/science.aac4919 [PubMed: 26184917]
56. Heinzel S et al. , A Myc-dependent division timer complements a cell-death timer to regulate T cell and B cell responses. Nat. Immunol 18, 96–103 (2017). doi: 10.1038/ni.3598 [PubMed: 27820810]
57. Bogdan JA et al. , Human carbon catabolite repressor protein (CCR4)-associative factor 1: Cloning, expression and characterization of its interaction with the B-cell translocation protein BTG1. Biochem. J 336, 471–481 (1998). doi: 10.1042/bj3360471 [PubMed: 9820826]
58. Yuniati L, Scheijen B, van der Meer LT, van Leeuwen FN, Tumor suppressors BTG1 and BTG2: Beyond growth control. J. Cell. Physiol 234, 5379–5389 (2019). doi: 10.1002/jcp.27407 [PubMed: 30350856]
59. Shen L, Shi Q, Wang W, Double agents: Genes with both oncogenic and tumor-suppressor functions. Oncogenesis 7, 25 (2018). doi: 10.1038/s41389-018-0034-x [PubMed: 29540752]
60. Datta N, Chakraborty S, Basu M, Ghosh MK, Tumor suppressors having oncogenic functions: The double agents. Cells 10, 46 (2020). doi: 10.3390/cells10010046 [PubMed: 33396222]
61. Waanders E et al. , The origin and nature of tightly clustered *BTG1* deletions in precursor B-cell acute lymphoblastic leukemia support a model of multiclonal evolution. PLOS Genet. 8, e1002533 (2012). doi: 10.1371/journal.pgen.1002533
62. Wu Y et al. , MicroRNA-17–92 is required for T-cell and B-cell pathogenicity in chronic graft-versus-host disease in mice. Blood 131, 1974–1986 (2018). doi: 10.1182/blood-2017-06-789321 [PubMed: 29530952]
63. Rouault JP et al. , BTG1, a member of a new family of antiproliferative genes. EMBO J. 11, 1663–1670 (1992). doi: 10.1002/j.1460-2075.1992.tb05213.x [PubMed: 1373383]
64. Venturutti L, Melnick AM, The dangers of déjà vu: Memory B cells as the cells of origin of ABC-DLBCLs. Blood 136, 2263–2274 (2020). doi: 10.1182/blood.2020005857 [PubMed: 32932517]

65. Becher B, Waisman A, Lu LF, Conditional gene-targeting in mice: Problems and solutions. Immunity 48, 835–836 (2018). doi: 10.1016/j.immuni.2018.05.002 [PubMed: 29768166]
66. Guide for the Care and Use of Laboratory Animals (The National Academies Press, ed. 8, 2011).
67. Inaba K et al. , Tissue distribution of the DEC-205 protein that is detected by the monoclonal antibody NLDC-145. I. Expression on dendritic cells and other subsets of mouse leukocytes. Cell. Immunol 163, 148–156 (1995). doi: 10.1006/cimm.1995.1109 [PubMed: 7758125]
68. Long JZ, Lackan CS, Hadjantonakis AK, Genetic and spectrally distinct *in vivo* imaging: Embryonic stem cells and mice with widespread expression of a monomeric red fluorescent protein. BMC Biotechnol. 5, 20 (2005). doi: 10.1186/1472-6750-5-20 [PubMed: 15996270]
69. Hanna J et al. , Direct reprogramming of terminally differentiated mature B lymphocytes to pluripotency. Cell 133, 250–264 (2008). doi: 10.1016/j.cell.2008.03.028 [PubMed: 18423197]
70. Pasqual G, Angelini A, Victora GD, Triggering positive selection of germinal center B cells by antigen targeting to DEC-205. Methods Mol. Biol 1291, 125–134 (2015). doi: 10.1007/978-1-4939-2498-1_10 [PubMed: 25836306]
71. Bankhead P et al. , QuPath: Open source software for digital pathology image analysis. Sci. Rep 7, 16878 (2017). doi: 10.1038/s41598-017-17204-5 [PubMed: 29203879]
72. Schindelin J et al. , Fiji: An open-source platform for biological-image analysis. Nat. Methods 9, 676–682 (2012). doi: 10.1038/nmeth.2019 [PubMed: 22743772]
73. Yang X et al. , A public genome-scale lentiviral expression library of human ORFs. Nat. Methods 8, 659–661 (2011). doi: 10.1038/nmeth.1638 [PubMed: 21706014]
74. Caeser R et al. , Genetic modification of primary human B cells to model high-grade lymphoma. Nat. Commun 10, 4543 (2019). doi: 10.1038/s41467-019-12494-x [PubMed: 31586074]
75. Huppertz I et al. , iCLIP: Protein–RNA interactions at nucleotide resolution. Methods 65, 274–287 (2014). doi: 10.1016/j.ymeth.2013.10.011 [PubMed: 24184352]
76. Carlson CS et al. , Using synthetic templates to design an unbiased multiplex PCR assay. Nat. Commun 4, 2680 (2013). doi: 10.1038/ncomms3680 [PubMed: 24157944]
77. Dobin A et al. , STAR: Ultrafast universal RNA-seq aligner. Bioinformatics 29, 15–21 (2013). doi: 10.1093/bioinformatics/bts635 [PubMed: 23104886]
78. Liao Y, Smyth GK, Shi W, The R package *Rsubread* is easier, faster, cheaper and better for alignment and quantification of RNA sequencing reads. Nucleic Acids Res. 47, e47 (2019). doi: 10.1093/nar/gkz114 [PubMed: 30783653]
79. Robinson MD, McCarthy DJ, Smyth GK, edgeR: A Bioconductor package for differential expression analysis of digital gene expression data. Bioinformatics 26, 139–140 (2010). doi: 10.1093/bioinformatics/btp616 [PubMed: 19910308]
80. McCarthy DJ, Chen Y, Smyth GK, Differential expression analysis of multifactor RNA-Seq experiments with respect to biological variation. Nucleic Acids Res. 40, 4288–4297 (2012). doi: 10.1093/nar/gks042 [PubMed: 22287627]
81. Csardi G, Nepusz T, The igraph software package for complex network research. InterJournal Complex Systems, 1695 (2006).
82. Goodarzi H, Elemento O, Tavazoie S, Revealing global regulatory perturbations across human cancers. Mol. Cell 36, 900–911 (2009). doi: 10.1016/j.molcel.2009.11.016 [PubMed: 20005852]
83. Shaffer AL et al. , A library of gene expression signatures to illuminate normal and pathological lymphoid biology. Immunol. Rev 210, 67–85 (2006). doi: 10.1111/j.0105-2896.2006.00373.x [PubMed: 16623765]
84. Johnson WE, Li C, Rabinovic A, Adjusting batch effects in microarray expression data using empirical Bayes methods. Biostatistics 8, 118–127 (2007). doi: 10.1093/biostatistics/kxj037 [PubMed: 16632515]
85. Leek JT, Johnson WE, Parker HS, Jaffe AE, Storey JD, The sva package for removing batch effects and other unwanted variation in high-throughput experiments. Bioinformatics 28, 882–883 (2012). doi: 10.1093/bioinformatics/bts034 [PubMed: 22257669]
86. Kulakovskiy IV et al. , HOCOMOCO: Towards a complete collection of transcription factor binding models for human and mouse via large-scale ChIP-Seq analysis. Nucleic Acids Res. 46, D252–D259 (2018). doi: 10.1093/nar/gkx1106 [PubMed: 29140464]

87. Bailey TL et al. , MEME SUITE: Tools for motif discovery and searching. Nucleic Acids Res. 37, W202–W208 (2009). doi: 10.1093/nar/gkp335 [PubMed: 19458158]
88. Bailey TL, Machanick P, Inferring direct DNA binding from ChIP-seq. Nucleic Acids Res. 40, e128 (2012). doi: 10.1093/nar/gks433 [PubMed: 22610855]
89. Risso D, Ngai J, Speed TP, Dudoit S, Normalization of RNA-seq data using factor analysis of control genes or samples. Nat. Biotechnol 32, 896–902 (2014). doi: 10.1038/nbt.2931 [PubMed: 25150836]
90. Stuart T et al. , Comprehensive integration of single-cell data. Cell 177, 1888–1902.e21 (2019). doi: 10.1016/j.cell.2019.05.031 [PubMed: 31178118]
91. Street K et al. , Slingshot: Cell lineage and pseudotime inference for single-cell transcriptomics. BMC Genomics 19, 477 (2018). doi: 10.1186/s12864-018-4772-0 [PubMed: 29914354]
92. Garcia M et al. , Sarek: A portable workflow for whole-genome sequencing analysis of germline and somatic variants. F1000Res. 9, 63 (2020). doi: 10.12688/f1000research.16665.2 [PubMed: 32269765]
93. Kim S et al. , Strelka2: Fast and accurate calling of germline and somatic variants. Nat. Methods 15, 591–594 (2018). doi: 10.1038/s41592-018-0051-x [PubMed: 30013048]
94. Chen X et al. , Manta: Rapid detection of structural variants and indels for germline and cancer sequencing applications. Bioinformatics 32, 1220–1222 (2016). doi: 10.1093/bioinformatics/btv710 [PubMed: 26647377]
95. Shamsani J et al. , A plugin for the Ensembl Variant Effect Predictor that uses MaxEntScan to predict variant spliceogenicity. Bioinformatics 35, 2315–2317 (2019). doi: 10.1093/bioinformatics/bty960 [PubMed: 30475984]
96. Imielinski M, Guo G, Meyerson M, Insertions and deletions target lineage-defining genes in human cancers. Cell 168, 460–472.e14 (2017). doi: 10.1016/j.cell.2016.12.025 [PubMed: 28089356]
97. Jiang Y et al. , *CREBBP* inactivation promotes the development of HDAC3-dependent lymphomas. Cancer Discov. 7, 38–53 (2017). doi: 10.1158/2159-8290.CD-16-0975 [PubMed: 27733359]
98. Whyte WA et al. , Master transcription factors and mediator establish super-enhancers at key cell identity genes. Cell 153, 307–319 (2013). doi: 10.1016/j.cell.2013.03.035 [PubMed: 23582322]
99. Pearson TA, Manolio TA, How to interpret a genome-wide association study. JAMA 299, 1335–1344 (2008). doi: 10.1001/jama.299.11.1335 [PubMed: 18349094]
100. Giudicelli V, Chaume D, Lefranc MP, IMGT/GENE-DB: A comprehensive database for human and mouse immunoglobulin and T cell receptor genes. Nucleic Acids Res. 33, D256–D261 (2005). doi: 10.1093/nar/gki010 [PubMed: 15608191]
101. Ye J, Ma N, Madden TL, Ostell JM, IgBLAST: An immunoglobulin variable domain sequence analysis tool. Nucleic Acids Res. 41, W34–W40 (2013). doi: 10.1093/nar/gkt382 [PubMed: 23671333]
102. Gupta NT et al. , Change-O: A toolkit for analyzing large-scale B cell immunoglobulin repertoire sequencing data. Bioinformatics 31, 3356–3358 (2015). doi: 10.1093/bioinformatics/btv359 [PubMed: 26069265]
103. Nouri N, Kleinstein SH, A spectral clustering-based method for identifying clones from high-throughput B cell repertoire sequencing data. Bioinformatics 34, i341–i349 (2018). doi: 10.1093/bioinformatics/bty235 [PubMed: 29949968]
104. Gupta NT et al. , Hierarchical clustering can identify B cell clones with high confidence in Ig repertoire sequencing data. J. Immunol 198, 2489–2499 (2017). doi: 10.4049/jimmunol.1601850 [PubMed: 28179494]
105. Yaari G et al. , Models of somatic hypermutation targeting and substitution based on synonymous mutations from high-throughput immunoglobulin sequencing data. Front. Immunol 4, 358 (2013). doi: 10.3389/fimmu.2013.00358 [PubMed: 24298272]
106. Hoehn KB, Pybus OG, Kleinstein SH, Phylogenetic analysis of migration, differentiation, and class switching in B cells. PLOS Comput. Biol 18, e1009885 (2022). doi: 10.1371/journal.pcbi.1009885
107. Nielsen R, Yang Z, Likelihood models for detecting positively selected amino acid sites and applications to the HIV-1 envelope gene. Genetics 148, 929–936 (1998). doi: 10.1093/genetics/148.3.929 [PubMed: 9539414]

108. Yu G, Lam TT, Zhu H, Guan Y, Two methods for mapping and visualizing associated data on phylogeny using *Ggtree*. Mol. Biol. Evol 35, 3041–3043 (2018). doi: 10.1093/molbev/msy194 [PubMed: 30351396]

109. Binder SC, Meyer-Hermann M, Implications of intravital imaging of murine germinal centers on the control of B cell selection and division. Front. Immunol 7, 593 (2016). doi: 10.3389/fimmu.2016.00593 [PubMed: 28066409]

110. Meyer-Hermann M, Overcoming the dichotomy of quantity and quality in antibody responses. J. Immunol 193, 5414–5419 (2014). doi: 10.4049/jimmunol.1401828 [PubMed: 25355924]

111. Meyer-Hermann M et al. , A theory of germinal center B cell selection, division, and exit. Cell Rep. 2, 162–174 (2012). doi: 10.1016/j.celrep.2012.05.010 [PubMed: 22840406]

112. Perelson AS, Oster GF, Theoretical studies of clonal selection: Minimal antibody repertoire size and reliability of self-non-self discrimination. J. Theor. Biol 81, 645–670 (1979). doi: 10.1016/0022-5193(79)90275-3 [PubMed: 94141]

113. Mlynarczyk C et al. , Codes used in “BTG1 mutation yields supercompetitive B cells primed for malignant transformation,” version 1.0.0, Zenodo (2022); 10.5281/zenodo.7406382.

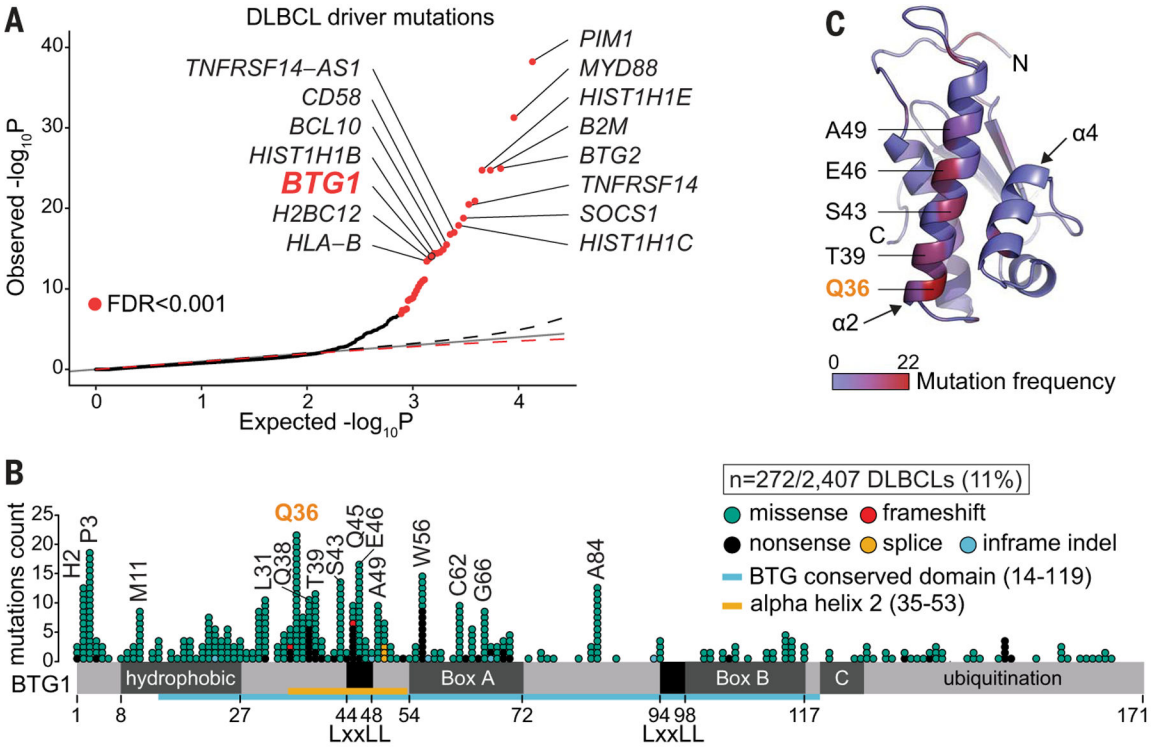

Fig. 1. Characterization of *BTG1* missense mutations in DLBCL.

(A) Quantile-quantile plot of observed and expected *P* values from a gamma-Poisson distribution for single nucleotide variants across 101 germline-matched whole genome–sequenced DLBCLs. Mutated genes with FDR < 0.001 are depicted with a red dot. (**B**) BTG1 protein and frequency, type, and location of mutations in $n = 272$ unique cases out of $n = 2407$ DLBCLs. LxxLL motifs mediate interaction with nuclear receptors. (**C**) BTG1 homology model (residues 1 to 129) based on a structural reference of BTG2 (Protein Data Bank ID 3DJU) showing mutation frequency. N- and C-terminal ends are denoted. Single-letter abbreviations for the amino acid residues are as follows: A, Ala; C, Cys; D, Asp; E, Glu; F, Phe; G, Gly; H, His; I, Ile; K, Lys; L, Leu; M, Met; N, Asn; P, Pro; Q, Gln; R, Arg; S, Ser; T, Thr; V, Val; W, Trp; and Y, Tyr.

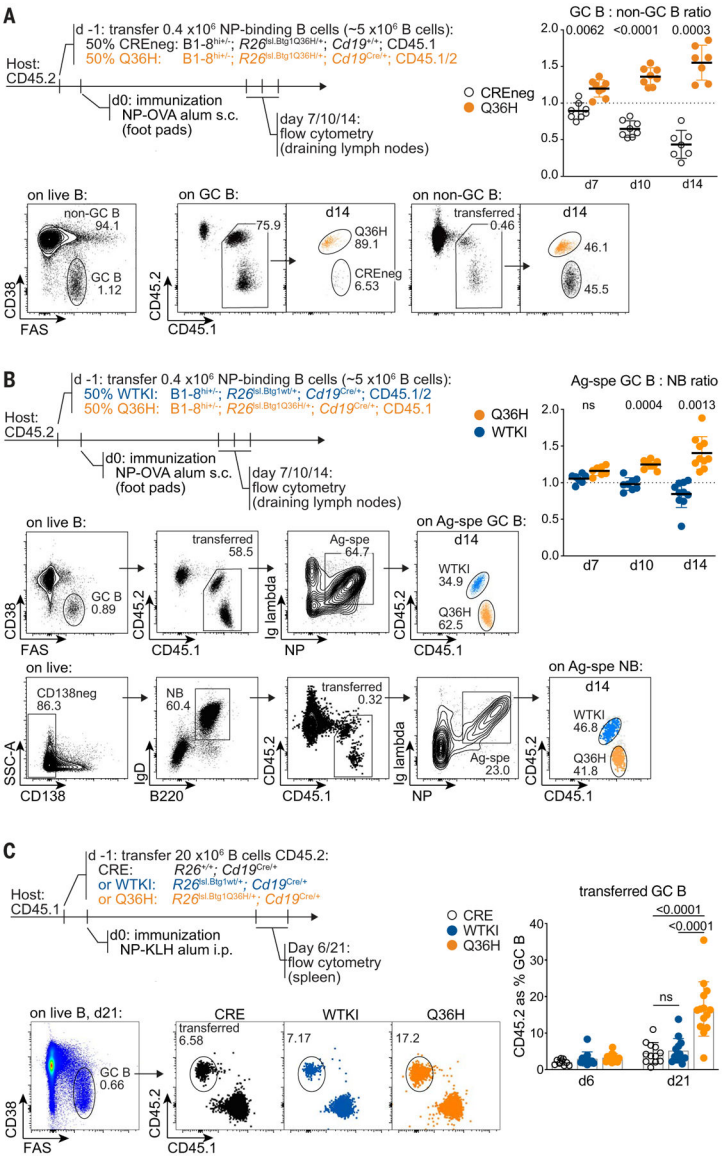

Fig. 2. Btg1^{Q36H} generates supercompetitor GC B cells.

(A) In vivo competitive assay schematic and representative flow cytometry plots for gating Q36H and CREneg from transferred germinal center (GC) B and non-GC B cells. Graph represents pooled mice from three independent experiments, each with $n = 2$ or 3 mice per time point. Mean ± SD, paired *t* test (two-tailed). **(B)** Competitive assay between mature B cells expressing Btg1^{Q36H} versus Btg1^{WT} from *Rosa26* (*R26*) knock-in alleles that differ by a single nucleotide. Representative flow cytometry plots for gating antigen-specific (Ag-spe, lambda^{+}NP^{+}) naïve B (NB, CD138^{-}B220^{+}IgD^{+}) and GC B (FAS^{+}CD38^{-}) WTKI and Q36H cells at day 14 after immunization. Graph represents pooled mice from two independent experiments, representative of three [day 7 (d7) and d14] or two (d10) independent experiments, each with $n = 3$ to 5 mice per time point. Mean ± SD, paired *t* test (two-tailed). **(C)** Experimental schematic for the adoptive transfer of B cells with an endogenous B cell receptor repertoire to compete with wild-type recipient cells. Representative flow cytometry

plots on live B cells (DAPI-B220^{+}) at day 21 after NP-KLH immunization, for gating transferred cells (CD45.2) of the indicated genotypes within GC B cells. Graph represents mice combined from three independent experiments, with 9 to 14 mice total per genotype and time point. Mean ± SD, unpaired *t* test (equal SD, two-tailed). s.c., subcutaneously.

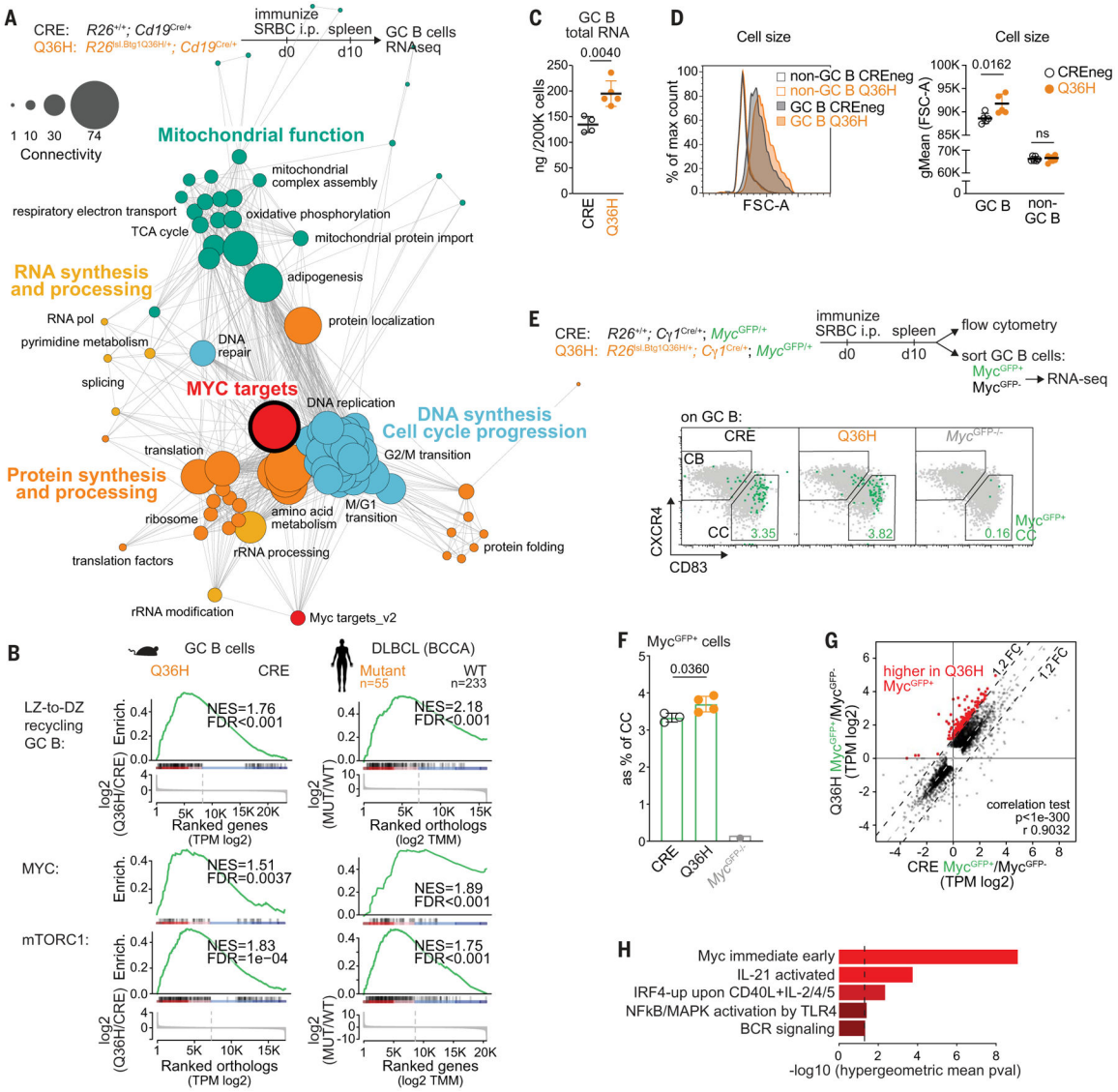

Fig. 3. Mutant BTG1 induces MYC-related biosynthetic programs.

(A) Gene set enrichment analysis (GSEA) network showing canonical and hallmark gene sets positively enriched in Q36H versus CRE up-regulated genes [normalized enrichment score (NES) ≥ 1.25; FDR < 0.05]. Distance between two enriched gene sets was calculated as the Jaccard index (size intersection: size union) using leading-edge genes. The circle size represents the degree of connectivity to which each gene set is attached to others. **(B)** GSEAs showing LZ-to-DZ recycling GC B, MYC, and mTORC1 activation signatures enrichment in Q36H versus CRE mouse GC B cells (left) and in BTG1 mutant versus WT DLBCL cases in the BC Cancer Agency (BCCA) cohort (right) (23). LZ-to-DZ recycling GC B signature is DECP_UPREG [*n* = 221 mouse genes (left); *n* = 201 human orthologs (right)]; MYC signature is SCHUHMACHER_MYC_TARGETS_UP [*n* = 80 mouse orthologs (left); *n* = 75 genes represented in the BCCA dataset (right)]; mTORC1 signature is PENG_RAPAMYCIN_RESPONSE_DN [*n* =242 mouse orthologs (left); *n* = 230 genes represented in the BCCA dataset (right)]. Enrich., enrichment score. **(C)** Graph

showing quantification of RNA extracted from 200,000 mouse GC B cells. One experiment, $n = 4$ and 5 mice per genotype. Mean ± SD, unpaired t test (equal SD, two-tailed). **(D)** Representative flow cytometry histograms showing cell size measurement as forward scatter area (FSC-A) in GC B (FAS^+CD38^-) and non-GCB (FAS^-CD38^+) cells (left). Graph showing geometric mean (gMean) of FSC-A from one experiment, $n = 5$ and 6 mice per genotype, representative of at least three independent experiments (right). Mean ± SD, unpaired t tests (two-tailed). **(E)** Experimental schematic and representative flow cytometry plots showing Myc^{GFP+} cells (green) in centroblasts (CB) and centrocytes (CC). **(F)** Bar plot showing proportion of Myc^{GFP+} cells in CC. One experiment with $n = 3$ and 4 mice per genotype, representative of at least three independent experiments. Mean ± SD, unpaired t test (two-tailed). **(G)** Genes ($n = 201$) depicted with red dots present higher expression (FC > 1.2) in GFP^{Myc+} versus GFP^{Myc-} GC B cells comparing Q36H mice (y axis) to CRE mice (x axis). **(H)** Hypergeometric mean analysis for the 201 genes identified in (G). The Myc immediate early signature consists of Myc-dependent genes induced by 8 hours in Myc WT/flox B cells (39). Genes in this and other gene signatures are included in supplementary table S4.

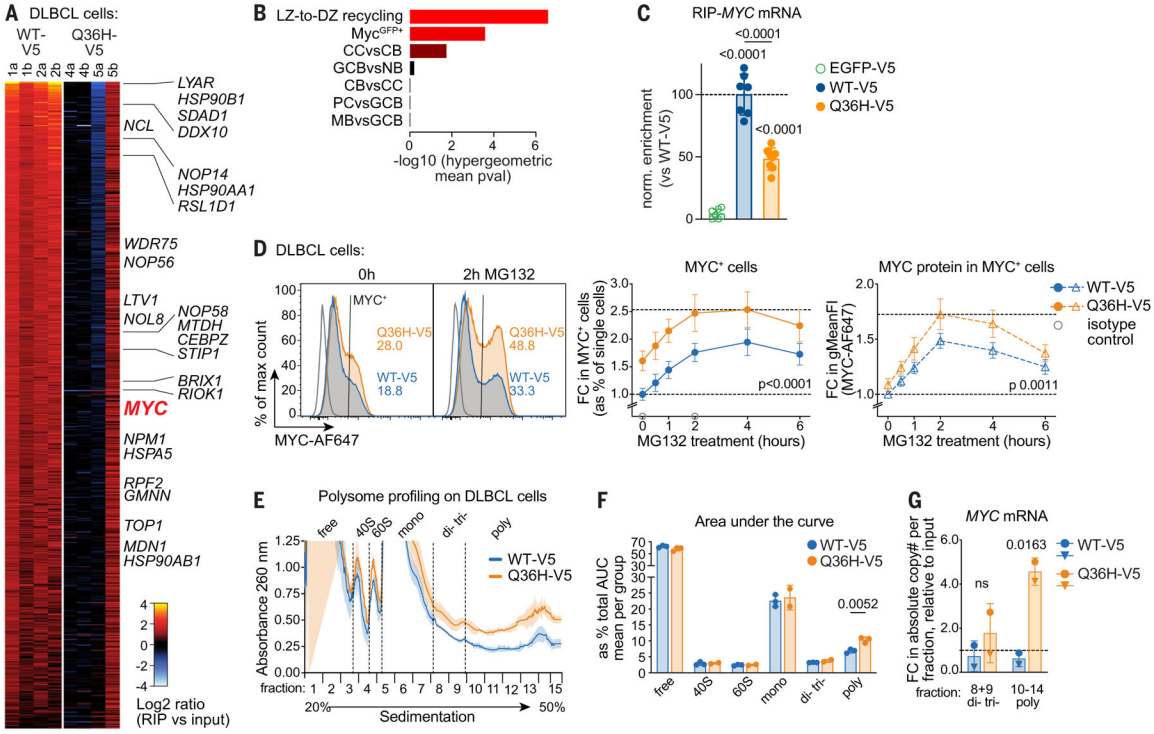

Fig. 4. Q36H mutation disrupts BTG1-*MYC* mRNA association and enhances MYC protein synthesis kinetics.

(A) Heatmap showing $n = 732$ BTG1^{WT}-associated (BTG1^{WT} RIP/input log2FC > 2, $q < 0.05$) and BTG1^{Q36H}-lost (BTG1^{Q36H}/BTG1^{WT} log2FC > 2, $q < 0.05$) transcripts by RIP-seq, using V5 antibody in SU-DHL4 DLBCL cells overexpressing V5-tagged BTG1^{WT} or BTG1^{Q36H}. *MYC* and leading edge genes from positively enriched LZ-to-DZ recycling GC B, MYC, and mTORC1 signatures in BTG1^{Q36H} versus BTG1^{WT} are labeled. **(B)** Signatures enriched for up-regulation of the $n = 732$ BTG1^{WT}-associated and BTG1^{Q36H}-lost transcripts as determined by hypergeometric mean analysis. **(C)** RIP-qPCR for *MYC* mRNA in indicated SU-DHL4 V5-tagged DLBCL cells. Mean ± SD of enrichment in RIP over input samples, normalized to BTG1^{WT}-V5. Three independent experiments, each with $n = 2$ or 3 independently generated lines per genotype. Unpaired *t* test (equal SD, two-tailed, versus EGFP or as indicated). **(D)** Representative MYC flow cytometry histograms of SU-DHL4 DLBCL cells expressing V5-tagged BTG1^{WT} (WT-V5) or BTG1^{Q36H} (Q36H-V5) and treated with 5 μM MG132 for 0 or 2 hours. Proportions of MYC-positive cells (MYC^{+}) are indicated. Staining with isotype control is included. Graphs show proportion of MYC^{+} cells (left) or MYC protein levels within MYC^{+} cells (right) as measured by flow cytometry in three independent experiments, each with $n = 2$ or 3 independently generated lines per genotype, shown as fold change relative to WT-V5 0 hour mean value per experiment. Mean ± SD, two-way analysis of variance (ANOVA) for Q36H-V5 versus WT-V5. gMeanFI, geometric mean fluorescence intensity. **(E)** Polysome profile of BTG1^{WT}-V5 and BTG1^{Q36H}-V5 expressing SU-DHL4 cells. Mean (line) ± SD (shade) from $n = 3$ independently generated lines per genotype except fractions 4 to 9: $n = 2$ Q36H lines owing to technical loss of one line. One experiment representative of two independent experiments. **(F)** Bar plot shows the area under the curve (AUC) for indicated portions of the

polysomal traces from (E), as percent of the total AUC average per genotype. Mean ± SD, unpaired *t* test (equal SD, two-tailed). **(G)** Absolute *MYC* mRNA levels from fractions in (E) and (F), pooled as indicated. $n = 2$ independently generated lines per genotype. Mean ± SD, unpaired *t* test (equal SD, two-tailed).

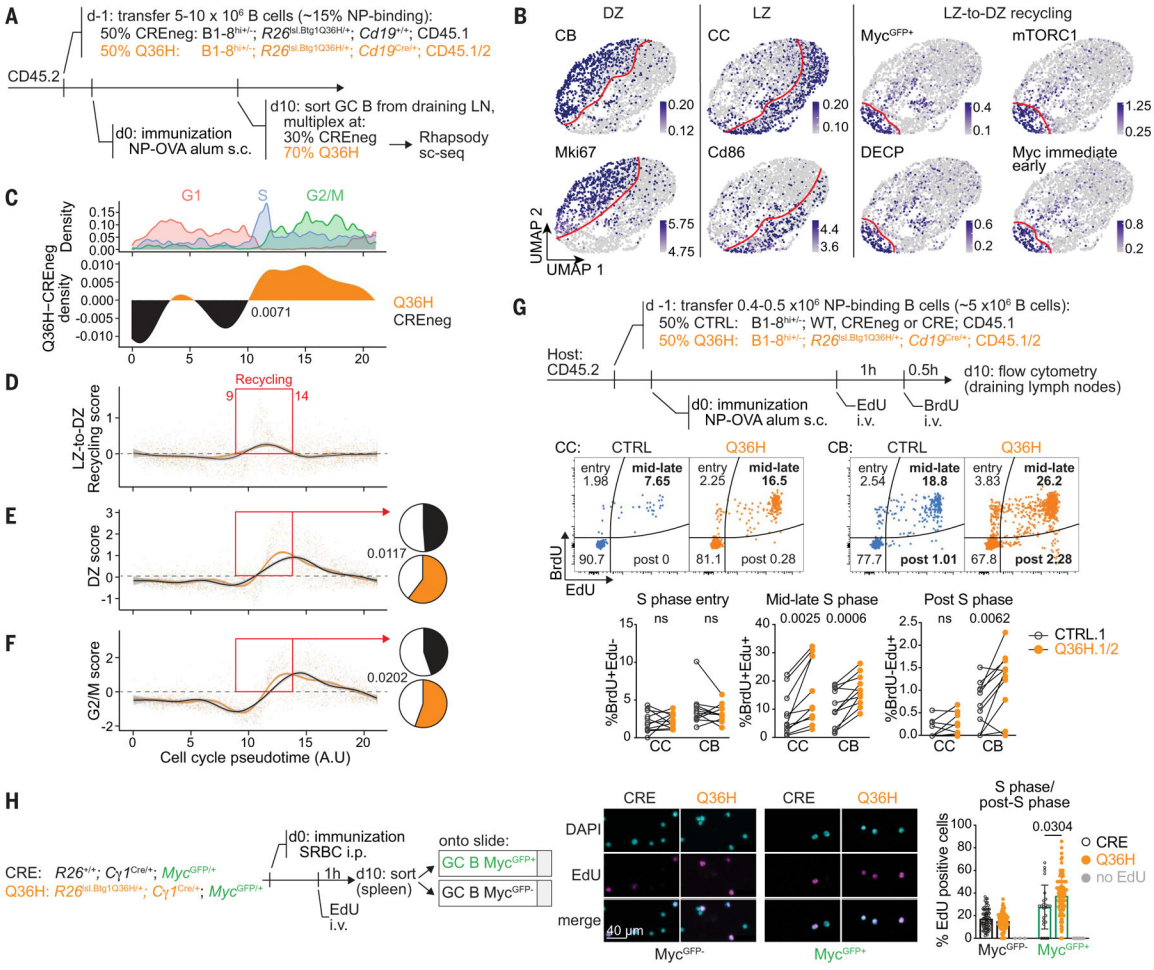

Fig. 5. Faster S phase completion and DZ program commitment in Btg1^{Q36H} LZ-to-DZ recycling cells.

(A) Experimental design for targeted single-cell RNA sequencing for $n = 496$ genes in competing Q36H and CREneg GC B cells from $n = 4$ mice pooled into three biological replicates. **(B)** Dark zone (DZ), light zone (LZ), and LZ-to-DZ recycling GC B cells were defined on the basis of signatures enrichment and of *Mki67* and *Cd86* marker expression levels, projected onto the uniform manifold approximation and projection (UMAP) distribution of cells ($n = 2982$). Centroblast (CB) and centrocyte (CC) signatures correspond to genes down-regulated or up-regulated in CC versus CB, respectively. Myc^{GFP+} signature represent genes up-regulated in Myc^{GFP+} versus Myc^{GFP-} CRE control GC B cells from Fig. 3E; mTORC1 signature is PENG_RAPAMYCIN_RESPONSE_DN; DECP signature is LZ_DECP_upreg and Myc immediate early signature consists of Myc-dependent genes induced by 8 hours in Myc WT/flox B cells. Genes in these signatures are included in table S4. **(C)** Distribution of cells enriched for G1, S, and G2/M signatures (top) and of Q36H and CREneg GC B cells differential density across a Slingshot cell cycle pseudotime axis. Difference in distribution of Q36H and CREneg cells by Wilcoxon test. (D to F) Distribution of Q36H and CREneg GC B cells based on their enrichment for **(D)** LZ-to-DZ recycling GC B signature, **(E)** DZ signature, or **(F)** G2/M signature, across the Slingshot cell cycle pseudotime axis. (D) Pseudotime units 9 to 14 correspond to LZ-to-DZ recycling GC cells

(score > 0). [(E) and (F)] Pie charts represent Q36H or CREneg GC B cells with (E) a DZ score > 0 or (F) a G2/M score > 0, as a proportion of LZ-to-DZ recycling cells (pseudotime units 9 to 14) from (D). Chi-square *P* value. **(G)** Experimental design for in vivo cell cycle profiling by EdU/BrdU dual staining of competing Q36H and CTRL GC B cells (top). Representative flow cytometry plots for CC and CB in S phase, mid-late S phase, and post S phase (middle). Graphs show data pooled from three independent experiments, with n = 3 or 4 mice each (bottom). Mean ± SD, paired *t* test (two-tailed). **(H)** Experimental design to measure S phase-experienced Q36H and CRE Myc^{GFP+} cells in vivo by EdU staining coupled with immunofluorescence (IF). Representative IF images are shown. Bar plot shows quantification from two independent experiments, each with n = 2 or 5 mice per genotype. Each dot represents one individual field of view with a minimum five cells per field of view. Mean ± SD, unpaired *t* test (two-tailed).

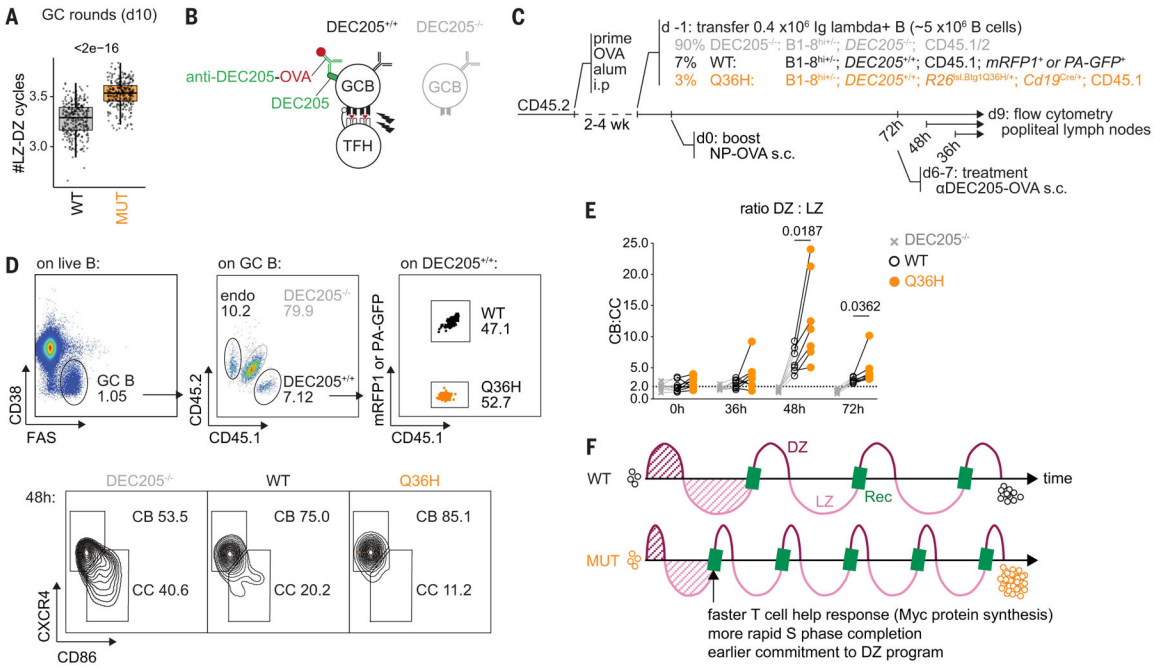

Fig. 6. Accelerated LZ-DZ recycling kinetics in Btg1^{Q36H} GC B cells.

(A) In silico readout for the number of LZ-DZ cycles undergone by competing Btg1 mutant versus WT GC B cells at day 10 after immunization, using the GC mathematical model in which mutant GC B cells are provided with 1.12 times faster T cell help response (faster up-regulation of Myc and mTORC1) and 21% shorter S phase. Each dot is a readout from a single simulation (n = 300). Difference by Wilcoxon test considering the mutant and WT readout from the same simulation as paired samples. (**B**) Schematic of the system used to deliver targeted T_{FH} cell help to competing GC B cells in vivo. (**C**) Experimental design for the targeted delivery of T_{FH} cell help to competing DEC205$^{+/+}$ WT and Q36H GC B cells in vivo and tracking their centroblast (CB) versus centrocyte (CC) identity over time. (**D**) Representative gating flow cytometry plots for C. (**E**) Graph shows pooled data for (C) and (D), from two experiments, each with n = 3 to 5 mice per time point. Paired t test, two-tailed. (**F**) Schematic model. More-rapid GC LZ-DZ cycles in Btg1 mutant (MUT) GC B cells, because of faster response to T_{FH} cell help via accelerated Myc protein induction, more rapid S phase completion and earlier commitment to DZ transcriptional program, explain the progressive competitive fitness gain of Btg1^{Q36H} GC B cells over the course of the GC reaction. Rec, LZ-to-DZ recycling.

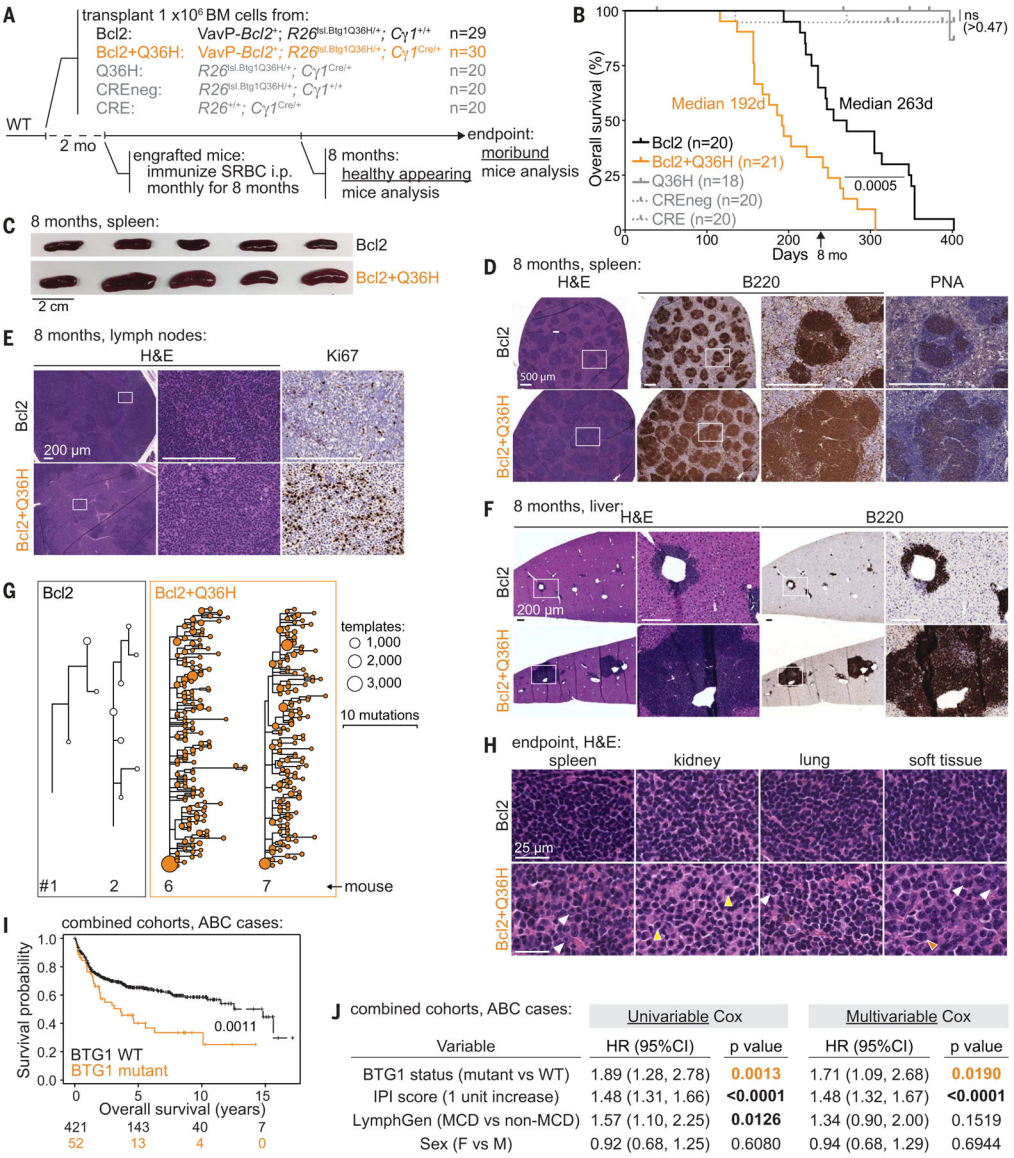

J combined cohorts, ABC cases:

	Univariable Cox		Multivariable Cox	
Variable	HR (95%CI)	p value	HR (95%CI)	p value
BTG1 status (mutant vs WT)	1.89 (1.28, 2.78)	**0.0013**	1.71 (1.09, 2.68)	**0.0190**
IPI score (1 unit increase)	1.48 (1.31, 1.66)	**<0.0001**	1.48 (1.32, 1.67)	**<0.0001**
LymphGen (MCD vs non-MCD)	1.57 (1.10, 2.25)	**0.0126**	1.34 (0.90, 2.00)	0.1519
Sex (F vs M)	0.92 (0.68, 1.25)	0.6080	0.94 (0.68, 1.29)	0.6944

Fig. 7. Mutant BTG1 drives formation of highly aggressive B cell lymphomas in mice and humans.

(A) Experimental design for testing contribution of the *R26*$^{lsl.Btg1Q36H/+}$ allele to Bcl2-driven lymphomagenesis. **(B)** Kaplan-Meier curves depicting overall survival of groups described in (A) in days after transplantation, assessed by either time of death or euthanasia upon sickness development. Log-rank (Mantel-Cox) test performed as indicated. **(C)** Image of $n = 5$ spleens per group at 8 months after transplantation. **(D)** Consecutive spleen sections from Bcl2 and Bcl2+Q36H mice at 8 months after transplantation stained with H&E or by immunohistochemistry (IHC) for B cells (B220 antibody) or GC B cells (PNA). Representative of $n = 5$ mice per genotype. **(E)** Consecutive lymph node sections from Bcl2 and Bcl2+Q36H mice at 8 months after transplantation stained with H&E or by IHC for proliferating cells (Ki67). Representative of $n = 5$ mice per genotype. **(F)** Consecutive liver sections from Bcl2 and Bcl2+Q36H mice at 8 months after transplantation stained with H&E or by IHC for B cells (B220). Representative of $n = 4$ mice per genotype. **(G)** B cell

lineage trees from BCR sequences analysis (ImmunoSeq) in Bcl2 and Bcl2+Q36H mice at 8 months after transplantation. The B cell clone with the most sequence reads for each mouse (mouse number indicated in the bottom) is shown. Branch lengths represent the estimated number of somatic hypermutations between nodes. Scale bar denotes 10 mutational events. Trees from $n = 2$ mice, representative of $n = 5$ mice per genotype (fig. S16F), are shown. **(H)** H&E staining on indicated tissue sections from Bcl2 and Bcl2+Q36H moribund mice. Representative of $n = 6$ mice per genotype. Low-grade follicular lymphoma–like centrocytes shown in Bcl2 mice. In Bcl2+Q36H mice, white arrowheads depict large immunoblastic cells; yellow, plasmacytoid cells; and orange, a large-size DLBCL-like cell. **(I)** Kaplan-Meier curves depicting overall survival of ABC-DLBCL patients combined from publicly available cohorts (9, 23, 24), based on their *BTG1* status. Log-rank test was performed. Censored events are indicated below the graph. **(J)** Univariate and multivariate analyses in ABC-DLBCL cases from the same combined cohorts as in (I). HR, hazard ratio with 95% confidence interval. *P* value from Wald chi-square test for H0:HR = 1.